



HAL
open science

A domain decomposition solver for large scale time-harmonic flow acoustics problems

Philippe Marchner, Hadrien Bériot, Sophie Le Bras, Xavier Antoine,
Christophe Geuzaine

► **To cite this version:**

Philippe Marchner, Hadrien Bériot, Sophie Le Bras, Xavier Antoine, Christophe Geuzaine. A domain decomposition solver for large scale time-harmonic flow acoustics problems. 2023. hal-04254633

HAL Id: hal-04254633

<https://hal.science/hal-04254633>

Preprint submitted on 23 Oct 2023

HAL is a multi-disciplinary open access archive for the deposit and dissemination of scientific research documents, whether they are published or not. The documents may come from teaching and research institutions in France or abroad, or from public or private research centers.

L'archive ouverte pluridisciplinaire **HAL**, est destinée au dépôt et à la diffusion de documents scientifiques de niveau recherche, publiés ou non, émanant des établissements d'enseignement et de recherche français ou étrangers, des laboratoires publics ou privés.

A DOMAIN DECOMPOSITION SOLVER FOR LARGE SCALE TIME-HARMONIC FLOW ACOUSTICS PROBLEMS

Abstract. This article is devoted to the numerical resolution of high frequency time-harmonic flow acoustic problems. We use a substructured optimized non-overlapping Schwarz domain decomposition method as a solver in order to significantly reduce the memory footprint required by such problems. To accelerate the convergence of the iterative solver we develop suitable transmission conditions based on local approximations of the Dirichlet-to-Neumann operator, taking into account convection by strongly non-uniform mean flows. The development relies on the construction of absorbing boundary conditions through microlocal analysis and pseudo-differential calculus. We analyze the potential of the method in academic settings and subsequently propose a robust domain decomposition methodology for problems of industrial relevance modelled by the Pierce linearized acoustic operator. The algorithm is implemented in an open-source high-order finite element library. It allows to solve challenging three-dimensional problems with more than one billion high-order unknowns, by taking full advantage of modern computer architectures.

Key words. Absorbing boundary conditions, optimized Schwarz method, high-performance computing, high frequency problems, Pierce operator, domain decomposition

AMS subject classifications. 35J05, 65N55, 68W10

1. Introduction. The reduction of noise emissions in the transport industry has become of increasing importance in the past decades. Noise simulation tools are crucial to support experimental techniques and lower the design cost of quiet technologies. The present work is motivated by aeroacoustics applications. Solving all the scales of the aeroacoustic problem requires tremendous numerical resolution and modeling effort. We focus instead on a hybrid approach, where the mean flow and acoustic perturbations are solved in separated steps. Such an approach is relevant in the context of aeroacoustics analogies (see e.g. [40, 51]), in which acoustic sources are extracted from a mean flow computation in a first step, and are propagated thanks to a wave-like partial differential equation in a second step. Various wave propagation models exist depending on the mean flow assumptions and presupposed flow-acoustic interactions. One of the most complete model for non-viscous flows without heat conduction and linear acoustic perturbations is the linearized Euler equations (LEEs). The LEEs support acoustic, hydrodynamic and entropy waves and their linear interactions. It is a vector partial differential equation describing five acoustic variables in three-dimensions, that remains costly and is subjected to numerical instabilities. We focus our study on the Pierce operator [57], which has the advantage to be described by a single scalar variable. It can provide an accurate alternative to the LEEs, especially in the high frequency limit [37]. Derived for arbitrary steady base flow, the operator is more general than the linearized potential equation from Goldstein [30] which is limited to potential homentropic mean flows. The Pierce operator has the advantage to be self-adjoint. Its resolution can be used as a black-box tool for optimization, compute tailored Green's functions or solve inversion problems such as sound source localization. We refer to the study initiated in [37] for more details.

The Pierce operator takes the form of a convected wave operator with variable coefficients

$$\mathcal{P} = -\rho_0 \frac{D}{Dt} \left(\frac{1}{\rho_0^2 c_0^2} \frac{D}{Dt} \right) + \nabla \cdot \left(\frac{1}{\rho_0} \nabla \right), \quad \frac{D}{Dt} = \partial_t + \mathbf{v}_0 \cdot \nabla,$$

where $\rho_0(\mathbf{x})$, $c_0(\mathbf{x})$ are respectively the density and speed of sound of the mean flow,

48 and $\mathbf{v}_0(\mathbf{x})$ is the vector velocity field, which is assumed to be subsonic so that the
 49 condition $\|\mathbf{v}_0(\mathbf{x})\|/c_0(\mathbf{x}) < 1$ holds. These quantities are data of the problem, which
 50 are computed in advance by a stationary flow solver, typically a Reynolds-averaged
 51 Navier–Stokes (RANS) solver. For a potential mean flow a non-linear Poisson solver
 52 can be used [28].

53 For turbomachinery applications it is customary to solve such a PDE in the
 54 frequency domain, because fixed frequency tones are often the main noise contribution
 55 [7]. Moreover porous material or acoustic liners are difficult to model in the time-
 56 domain. For all these reasons an efficient and accurate frequency-domain resolution
 57 of such an operator is critical, in particular at high frequencies.

58 At the mathematical level, time-harmonic wave propagation problems are noto-
 59 riously difficult to solve at high frequencies [23]. The usual variational formulation
 60 of such problems are complex-valued and strongly indefinite. The strong indefinit-
 61 ness of the problem leads to inefficient iterative solvers, and makes preconditioners
 62 challenging to design [22]. As a result, direct solvers are generally advocated in the in-
 63 dustry. High frequency problems face two major numerical difficulties: i) the number
 64 of discretization points per wavelength must grow significantly to avoid the pollution
 65 effect, especially for problem with flow convection [11]; ii) the memory requirement
 66 for direct solvers grows roughly as $\mathcal{O}(\omega^3)$ for a fixed numerical resolution, making high
 67 frequency problems out of reach in practice. The first difficulty has been significantly
 68 reduced thanks to the progress of high-order discretization methods. In this work we
 69 use a conformal high-order finite element discretization based on integrated Legendre
 70 polynomials [61]. Order adaptivity rules have been designed [12, 10] to leverage the
 71 pollution effect. The counterpart of using a high-order basis is the increase of the
 72 matrix filling, which induces a higher memory footprint.

73 The second difficulty is common to all discretization methods, where the com-
 74 puter memory dictates the high frequency limit that can be simulated. Solutions to
 75 time-harmonic PDEs are non-local in space and highly oscillatory, making most of nu-
 76 merical algorithms hard to parallelize. Direct solvers can take advantage of the linear
 77 system structure and use efficient distributed parallelism strategies based on graph
 78 partitioning methods [4]. While it provides significant speed ups, memory overhead
 79 and scalability limits the applicability of direct solvers to a large number of processes
 80 [38]. This is expected since a pure algebraic parallel approach requires the factoriza-
 81 tion of a fully populated Schur complement system. Improvements of direct solvers
 82 were achieved in the recent years thanks to Block-Low Rank compression [3] combined
 83 with mixed-precision arithmetic [1]. The applicability to large scale time-harmonic
 84 problems is an active research topic.

85 The purpose of this article is to address the second difficulty based on a domain
 86 decomposition strategy at the continuous level. We reformulate the Pierce radiation
 87 problem using an optimized Schwarz domain decomposition method [26, 6] posed on
 88 the partition interfaces, and propose a hybrid direct-iterative solver suitable for high
 89 frequency computations on a distributed memory architecture. The computational
 90 domain is split into independent non-overlapping subdomains where a direct solver is
 91 called, and the global interface problem is solved in parallel by an iterative method.
 92 In that way we take advantage of direct solvers for medium size problems, and rely on
 93 solving iteratively an interface problem of smaller size. The resolution of the interface
 94 problem amounts to solve a Schur complement system at the algebraic level.

95 Domain decomposition also inherits from the strong indefiniteness of time-harmonic
 96 problems. The original Schwarz method does not converge for such problems and the
 97 issue was resolved in the early 1990’s by Lions [41] and Després [17]. An appro-

98 puate choice of transmission conditions between the subdomains is required for fast
 99 convergence, which depends directly on the underlying PDE. The ideal transmission
 100 condition is given by the Dirichlet-to-Neumann (DtN) map relative to the complemen-
 101 tary of each subdomain, which is the continuous equivalent of the Schur complement.
 102 Major developments were made over the years in order to build local approximations
 103 of the DtN map and accelerate the convergence of the iterative solver, including opti-
 104 mal [26], high-order [15, 50], Perfectly Matched Layer (PML) based [21, 64, 60] or
 105 non-local [54] transmission operators. They act as a preconditioner for the global
 106 interface, Schur complement system. Let us mention that these developments are
 107 intimately related to the design of non-reflecting boundary conditions, as we will see
 108 in the article.

109 A global communication strategy, that allows to propagate information at a larger
 110 scale, is however necessary to achieve scalability with the number of subdomains.
 111 Sweeping preconditioners [70] or coarse space corrections [14] could be used for that
 112 purpose. We refer to [27] for a review and general discussion of the many existing
 113 approaches. Most of these developments were applied to the Helmholtz or Maxwell
 114 equations, but less work have been devoted to problems with convection and variable
 115 coefficients with the exception of [68]. The objective of the paper is to propose a
 116 robust domain decomposition approach for industrial radiation problems governed by
 117 the Pierce equation.

118 The article is organized as follows. Section 2 explains how to obtain a family of
 119 high-order absorbing boundary conditions (ABCs) accounting for strong convection
 120 and variable coefficients. In particular we show robustness of the ABCs at Mach num-
 121 bers close to 1 for a convex boundary shape, for which difficulties have been raised
 122 in the literature [31, 9]. The construction follows the pioneer approach from [20] and
 123 extends the work initiated in [45]. In Section 3, we apply the optimized Schwarz
 124 method to the Pierce operator, and propose suitable transmission operators inspired
 125 from the ABCs. We show the performance of the domain decomposition algorithm
 126 on academic problems, for which the performance is quasi-optimal for simple shaped
 127 interfaces as a direct extension to [15]. In Section 4, we highlight the challenges of
 128 applying the domain decomposition method in more realistic settings. We address
 129 the integration of complex boundary conditions and propose a practical methodol-
 130 ogy using a second order transmission operator to handle large scale high frequency
 131 problems. We demonstrate the scalability of the algorithm on medium size problems,
 132 before showcasing its ability to solve large scale problems of industrial relevance by
 133 computing the noise radiated by the intake and the exhaust of a high by-pass ratio
 134 aircraft engine. This leads to the solution of three-dimensional finite element prob-
 135 lems with more than a billion high-order unknowns on massively parallel, distributed
 136 memory architectures. We conclude by mentioning some perspectives and limitations.

137 **Notations.** Through all the article we use the $e^{+i\omega t}$ time-harmonic convention,
 138 with ω the angular frequency. We introduce the vector Mach number $\mathbf{M}(\mathbf{x}) =$
 139 $\mathbf{v}_0(\mathbf{x})/c_0(\mathbf{x})$, with $\mathbf{M} = (M_x, M_y, M_z)^T$ being its components in a local Cartesian
 140 coordinate system (x, y, z) . The Mach number is defined to be the positive scalar
 141 quantity $M = \|\mathbf{M}\|$, and we introduce the Prandtl-Glauert factor $\beta = \sqrt{1 - M^2}$.
 142 The local wavenumber is denoted $k_0 = \omega/c_0(\mathbf{x})$.

143 **2. Non-reflecting boundary conditions with convection and variable**
 144 **coefficients.** This section is devoted to the design of non-reflecting boundary condi-
 145 tions for flow acoustics. We focus our study on absorbing boundary conditions, that
 146 are more direct to use in a domain decomposition context compared to other domain

147 truncation techniques such as perfectly matched layers or infinite elements.

148 Many time-harmonic problems are posed in an unbounded domain. It is well-
 149 known that a Sommerfeld-like radiation condition must be satisfied at infinity in
 150 order to have a well-posed boundary value problem. Radiation conditions that take
 151 into account convection effects can be found in [37, 63, 13]. An accurate truncation of
 152 the computational domain must be devised for volume based discretization methods,
 153 which is not obvious in the presence of spatially varying mean flow properties.

154 Applying a radiation condition on a finite boundary leads a non-local Dirichlet-to-
 155 Neumann (DtN) map. In this section we adopt the point of view of pseudodifferential
 156 calculus and approximate the DtN map through its symbol, that allows us to propose
 157 high-order absorbing boundary conditions. We obtain the exact DtN map for the half-
 158 space convected Helmholtz problem, from which we deduce an approximation of the
 159 DtN map for the Pierce operator on a general convex boundary and arbitrary mean
 160 flow orientation. To implement the ABCs we use an operator localization procedure.
 161 We conclude the section by showing numerical results of a point source radiation
 162 problem with a Mach number close to 1.

163 **2.1. DtN map for Pierce operator.** We here derive the symbol of the DtN
 164 map for the outgoing wave associated to the Pierce partial differential operator. The
 165 starting point is the formal factorization of the operator along its characteristics rays
 166 using Nirenberg's factorization theorem [53]. The factorization guarantees that the
 167 rays are solutions to the Hamilton-Jacobi equations [33], such that the characteristics
 168 carry the group velocity of the wave. The theory has been extended in [43] for general
 169 operators with variable coefficients. The study of the rays for the Pierce equation can
 170 be found in [62, Chap. 2.7].

171 We work with the half-space domain $\Omega = \{\mathbf{x} \in \mathbb{R}^3; x \leq 0\}$ delimited by the
 172 vertical boundary $\Gamma = \{x = 0\}$. We highlight that the following derivation can
 173 be extended to curved boundaries using the tangent plane approximation in a local
 174 coordinate system $(\mathbf{n}, \boldsymbol{\tau}_1, \boldsymbol{\tau}_2)$ attached to Γ . Here \mathbf{n} is the outward unit normal to Γ ,
 175 and $(\boldsymbol{\tau}_1, \boldsymbol{\tau}_2)$ is an orthonormal basis to the tangent plane. In the half-space case we
 176 use the canonical basis of \mathbb{R}^3 . As a preliminary step we normalize the Pierce operator

$$177 \quad \mathcal{P}^*(\omega, \mathbf{x}, \partial_{\mathbf{x}}) = \frac{\rho_0}{(1 - M_x^2)} \mathcal{P}(\omega, \mathbf{x}, \partial_{\mathbf{x}}),$$

179 where $(1 - M_x^2) \neq 0$ because the mean flow is assumed to be subsonic. Since the
 180 Pierce operator is a second order operator, the Nirenberg's factorization theorem for
 181 the reflected wave states that there exists two pseudodifferential operators (Λ^+, Λ^-)
 182 of order $+1$ such that

$$183 \quad (2.1) \quad \mathcal{P}^* = (\partial_x + \imath\Lambda^+) (\partial_x + \imath\Lambda^-) + \mathcal{R},$$

185 where (Λ^+, Λ^-) are associated to respectively the outgoing and incoming characteris-
 186 tics rays, and $\mathcal{R} \in \text{OPS}^{-\infty}$ is a regularizing pseudodifferential operator following the
 187 definition in [65]. In order to cancel the outgoing reflected wave on the non-reflecting
 188 boundary Γ , we must satisfy the relation, for a wavefield u

$$189 \quad (2.2) \quad \partial_x u = -\imath\Lambda^+ u, \quad \text{on } \Gamma.$$

191 We can then define $\Lambda_{\Gamma}^+ := H^{1/2}(\Gamma) \rightarrow H^{-1/2}(\Gamma)$ to be the Dirichlet-to-Neumann map
 192 for the outgoing wave. We define the symbol λ^+ of Λ^+ as its partial Fourier integral

193 representation in the tangential coordinate system attached to Γ

$$194 \quad (2.3) \quad \Lambda^+ u = \int_{\mathbb{R}^2} \lambda^+(\boldsymbol{\tau}, \boldsymbol{\xi}) \hat{u}(\boldsymbol{\xi}) e^{i\boldsymbol{\tau} \cdot \boldsymbol{\xi}} d\boldsymbol{\xi}, \quad \boldsymbol{\tau} \in \Gamma,$$

195

196 where $\hat{u}(\boldsymbol{\xi})$ is the Fourier transform of u . We use the notation $\Lambda^+ = \text{Op}(\lambda^+)$ to
 197 relate the operator to its symbol. To find the form of the operator Λ^+ , we expand
 198 the factorization (2.1) and identify the first and zeroth order x -derivatives terms with
 199 the Pierce operator written in the local coordinate system (x, y, z) . After algebraic
 200 manipulations detailed in Appendix A, we obtain the operator equation

$$201 \quad (2.4) \quad (1 - M_x^2) ((\Lambda^+)^2 + i\text{Op}\{\partial_x \lambda^+\}) + i(\mathcal{A}_1 + \mathcal{A}_0)(\Lambda^+) = (\mathcal{B}_2 + \mathcal{B}_1).$$

203 The operators $(\mathcal{A}_1, \mathcal{A}_0)$ and $(\mathcal{B}_2, \mathcal{B}_1)$ are differential operators indexed by their degree
 204 of homogeneity with respect to $(\omega, \boldsymbol{\xi})$, because the angular frequency ω is interpreted
 205 as the symbol of the time-derivative. We have found a Ricatti-type equation for the
 206 operator Λ^+ , which is nothing but a reformulation of the Pierce equation as a one-way
 207 equation.

208 **2.2. Computation of the principal symbol.** The next step is to look for
 209 the symbol λ^+ instead of computing Λ^+ directly. To do so we work with the set of
 210 classical symbols introduced by Hörmander [33]. This allows to use the asymptotic
 211 expansion $\lambda^+ \sim \sum_{j=-1}^{\infty} \lambda_{-j}^+$, where each symbol is homogeneous of order $(-j)$ with
 212 respect to $(\omega, \boldsymbol{\xi})$. The equivalence class \sim means that the reminder is a symbol of
 213 rapid polynomial decay in $\boldsymbol{\xi}$, associated to a smooth integral operator. Concretely we
 214 can give a notion of ‘‘convergence’’ for pseudodifferential operator, which here takes
 215 the form of a high frequency limit.

216 Moreover we have a set of calculus rules for classical symbols that allows to
 217 obtain λ_{-j}^+ algebraically. Moving the operator equation (2.4) at the symbol level, we
 218 can identify the homogeneous second order terms thanks to the composition rule for
 219 pseudo-differential calculus [65],

$$220 \quad (1 - M_x^2)(\lambda_1^+)^2 + i\sigma(\mathcal{A}_1)\lambda_1^+ = \sigma(\mathcal{B}_2),$$

222 where $\sigma(\cdot)$ denotes the symbol of the operator. Solving the polynomial of degree two
 223 for λ^+ gives two possibilities for the principal symbol

$$224 \quad (2.5) \quad \lambda_1^+ = \frac{1}{1 - M_x^2} \left[-M_x(k_0 - \mathbf{M}_\boldsymbol{\tau} \cdot \boldsymbol{\xi}) \pm \sqrt{k_0^2 - 2k_0 \mathbf{M}_\boldsymbol{\tau} \cdot \boldsymbol{\xi} - \beta^2 |\boldsymbol{\xi}|^2} \right],$$

225

226 where $\mathbf{M}_\boldsymbol{\tau} = (M_y, M_z)^T$ is the vector Mach number projected onto the tangential
 227 basis. The expression matches the dispersion relation for a plane wave. To select the
 228 sign in front of the square-root we can simply look that at the high frequency limit
 229 $k_0 \rightarrow +\infty$, which gives $\lambda_1^+ \rightarrow k_0 \frac{-M_x \pm 1}{1 - M_x^2}$. Since we target a positive group velocity for
 230 the outgoing wave, we select the positive sign and find $\lambda_1^+ \rightarrow k_0/(1 + M_x)$. Another
 231 point of view consists in comparing λ_1^+ with the group velocity of a plane wave along
 232 the normal direction of the boundary, see [44]. Keeping the negative sign in front of the
 233 square-root gives the principal symbol λ_1^- associated to the incoming characteristic.
 234 It is possible in theory to find the next terms of the symbol asymptotic expansion, as
 235 done in [45] for a simplified case. In this article we simply keep the principal symbol,
 236 which amounts to truncate the expansion to the first term $\lambda^+ \approx \lambda_1^+$.

237 **2.3. Operator representation.** The next step is to find a suitable operator
 238 related to the principal symbol λ_1^+ . For the half-space problem with a uniform mean
 239 flow, it is natural to propose, using the inverse Fourier representation on Γ

(2.6)

$$240 \quad \text{Op}(\lambda_1^+) = \frac{1}{1 - M_x^2} \left[-M_x k_0 + i M_x (\mathbf{M}_\tau \cdot \nabla_\Gamma) + \sqrt{k_0^2 - 2i k_0 (\mathbf{M}_\tau \cdot \nabla_\Gamma) + \beta^2 \Delta_\Gamma} \right],$$

242 where ∇_Γ is the surface gradient and Δ_Γ is the Laplace-Beltrami operator. In this
 243 specific situation we have $\Lambda^+ = \text{Op}(\lambda_1^+) + \mathcal{R}$, $\mathcal{R} \in \text{OPS}^{-\infty}$. In the general case
 244 of a non-uniform mean flow, the developments reported in Appendix A show that
 245 mean flow variations are only involved in the first order homogeneous terms for the
 246 computation of the zeroth order symbol λ_0^+ . At the operator level, it implies $\Lambda^+ =$
 247 $\text{Op}(\lambda_1^+) \bmod \text{OPS}^0$, in other words both operators differ by a pseudo-differential
 248 operator of order 0. The same conclusion holds when Γ is a convex curved boundary
 249 [5].

250 To summarize, we have found a general high frequency approximation of the
 251 outgoing characteristic Λ^+ for the Pierce operator, valid for non-uniform mean flows
 252 in the tangent plane approximation. In a general curved boundary setting, we define
 253 our non-reflecting boundary condition for the outgoing wave through

$$254 \quad (2.7) \quad \partial_{\mathbf{n}} u = -i \Lambda_1^+ u, \quad \text{on } \Gamma, \quad \Lambda_1^+ = \text{Op}(\lambda_1^+).$$

256 **Remark.** It is worth mentioning that in some situations with variable coefficients
 257 one can exactly match the DtN symbol expansion. This occurs for example in the
 258 pure Helmholtz case where the coefficients vary only along the tangential directions.
 259 With $\mathbf{v}_0 = (0, 0, 0)^T$, $c_0(\mathbf{x}) = c_0(y, z)$, $\rho_0(\mathbf{x}) = \rho_0(y, z)$, the exact DtN map for the
 260 half-space problem is

$$261 \quad \Lambda^+ = \sqrt{k_0^2 + \rho_0 \nabla_\Gamma (\rho_0^{-1} \nabla_\Gamma)}, \quad \text{on } \Gamma.$$

263 We will show in Section 3 that a proper discretization of this operator is equivalent to
 264 a block LU factorization at the continuous level in a domain decomposition context.

265 **2.4. Construction of the ABCs.** The operator (2.6) is still non-local. We
 266 explain in this section how to obtain local families of ABCs, following a localization
 267 procedure of the square-root operator at high frequencies.

268 **Square-root approximation.** To build a hierarchy of absorbing boundary con-
 269 ditions, we heavily rely on approximating the square-root function

$$270 \quad f(z) = \sqrt{1+z}, \quad z \in \mathbb{C},$$

272 considering the determination along the principal branch-cut line $z \in \{-1, -\infty\}$. We
 273 can build approximations of f thanks to a truncated Taylor or Padé expansion around
 274 $z = 0$, which are however not valid along the branch-cut. This is problematic since
 275 we will see that the branch-cut line is associated to evanescent modes. Following [48]
 276 we circumvent this issue by introducing a rotation of the branch-cut along the ray
 277 $R = -1 + r e^{i(\pi+\alpha)}$, $r > 0$, $\alpha \in [0, -\pi]$, such that the approximation is done on the
 278 function $f_\alpha(z) = e^{i\alpha/2} \sqrt{e^{-i\alpha}(1+z)}$ that we rewrite under the form

$$279 \quad f_\alpha(z) = e^{i\alpha/2} \sqrt{1+z_\alpha}, \quad z_\alpha = e^{-i\alpha}(1+z) - 1.$$

280

281 We can now use a classic diagonal Padé or Taylor approximation of order $N \in \mathbb{N}$,
 282 and denote the resulting approximation respectively $f_{PN,\alpha}$ and $f_{TN,\alpha}$. We compute
 283 in Figure 2.1 the absolute error

$$284 \quad |f(x) - f_{\{T,P\}N,\alpha}(x)|, \quad x \in \mathbb{R},$$

286 and show the impact of the angle α on the approximation of f . We observe that
 287 choosing $\alpha = -\pi/2$ provides an uniform approximation along the real line except
 288 around the singular point $z = -1$. For a fixed order N , the choice $\alpha = 0$ leads to a
 better approximation when $z > -1$ but incorrectly captures the range $z < -1$.

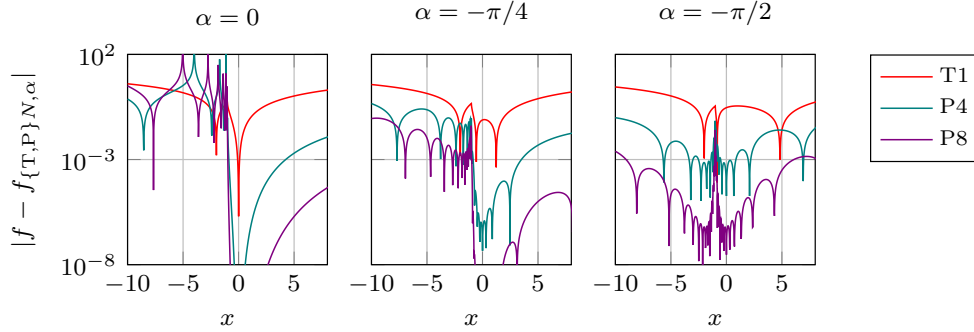


FIG. 2.1. Absolute error between f and $f_{\{T,P\}N,\alpha}$ along the real line.

289

290 **Localization of the DtN map.** The outgoing wave is of different nature de-
 291 pending on the sign of the radicand in the principal symbol (2.5), which is directly
 292 linked to microlocal regimes [43]. In order to capture the different regimes in a single
 293 approximation we first rewrite the operator (2.6) under the form $e^{i\alpha/2}\sqrt{1 + \mathcal{Z}_\alpha}$, where
 294 \mathcal{Z}_α is a second order differential operator. We have

$$295 \quad (2.8) \quad \Lambda_1^+ = \frac{-M_n k_0 + iM_n(\mathbf{M}_\tau \cdot \nabla_\Gamma) + k_0 e^{i\alpha/2} \sqrt{1 + \mathcal{Z}_\alpha}}{1 - M_n^2}, \quad \text{on } \Gamma,$$

$$296 \quad \text{with } \mathcal{Z}_\alpha = e^{-i\alpha}(1 + \mathcal{Z}) - 1, \quad \mathcal{Z} = -2i \frac{\mathbf{M}_\tau \cdot \nabla_\Gamma}{k_0} + \beta^2 \frac{\Delta_\Gamma}{k_0^2},$$

297

298 such that $\mathcal{Z} \rightarrow 0$ in the high frequency limit $\omega \rightarrow +\infty$. Using the square-root approx-
 299 imation at the operator level, we are able to approach Λ_1^+ for both the evanescent
 300 and propagative parts of the spectrum when $\alpha \in (0, -\pi)$. This localization method
 301 allows to maintain a sparse discrete system once the operator is discretized with finite
 302 elements. The resulting local ABCs will be referred to as Taylor or Padé ABCs, called
 303 respectively $\text{ABC}^{\text{TN},\alpha}$ and $\text{ABC}^{\text{PN},\alpha}$.

304 **2.5. Validation for a strong uniform mean flow.** The variational formula-
 305 tion associated to a Pierce boundary value problem is found by using Green's formula
 306 for the material derivative. For any test function $v \in V$, where $V \subset H^1(\Omega)$, we obtain

$$307 \quad \int_{\Omega} \left[\frac{1}{\rho_0} \nabla u \cdot \nabla v - \frac{1}{\rho_0 c_0^2} \frac{D_0 u}{Dt} \frac{D_0 v}{Dt} \right] d\Omega + \int_{\partial\Omega} \left[\frac{\mathbf{v}_0 \cdot \mathbf{n}}{\rho_0 c_0^2} \frac{D_0 u}{Dt} - \frac{1}{\rho_0} \frac{\partial u}{\partial \mathbf{n}} \right] \bar{v} ds = 0,$$

308

309 where \bar{v} is the complex conjugate, and we assumed no volume sources for conciseness.
 310 A total flux formulation is chosen to keep the formulation symmetric, see [9] for
 311 alternative definitions. Expanding the boundary term on the non-reflecting boundary
 312 Γ reads

$$313 \quad (2.9) \quad \frac{\mathbf{v}_0 \cdot \mathbf{n}}{\rho_0 c_0^2} \frac{D_0 u}{Dt} - \frac{1}{\rho_0} \frac{\partial u}{\partial \mathbf{n}} = \rho_0^{-1} i k_0 M_{\mathbf{n}} u + \rho_0^{-1} M_{\mathbf{n}} M_{\boldsymbol{\tau}} \frac{\partial u}{\partial \boldsymbol{\tau}} - \rho_0^{-1} (1 - M_{\mathbf{n}}^2) \frac{\partial u}{\partial \mathbf{n}}.$$

315 Replacing the normal derivative by the approximate DtN map Λ_1^+ from (2.8) results
 316 in an important simplification of the boundary integral:

$$317 \quad (2.10) \quad \int_{\Gamma} \left[\frac{\mathbf{v}_0 \cdot \mathbf{n}}{\rho_0 c_0^2} \frac{D_0 u}{Dt} - \frac{1}{\rho_0} \frac{\partial u}{\partial \mathbf{n}} \right] \bar{v} ds = \int_{\Gamma} i e^{i\alpha/2} \rho_0^{-1} k_0 \sqrt{1 + \mathcal{Z}_{\alpha} u} \bar{v} ds.$$

319 We immediately note that the ABC can be implemented in the same way as in the
 320 Helmholtz case [15, 67], albeit with an adjustment of the operator \mathcal{Z}_{α} . We then
 321 follow the usual implementation of high-order ABCs such as presented in [49]. In
 322 particular we introduce N auxiliary fields for the implementation of the Padé-based
 323 ABCs. Substituting the first order Taylor approximation $\Lambda_1^+ \approx \text{ABC}^{\text{T1},\alpha}$ in (2.10)
 324 leads a simple second order boundary operator

$$325 \quad \int_{\Gamma} \left[i \rho_0^{-1} k_0 \cos(\alpha/2) + \rho_0^{-1} e^{-i\alpha/2} \left(M_{\boldsymbol{\tau}} \nabla_{\Gamma} + i \frac{\beta^2}{2k_0} \Delta_{\Gamma} \right) \right] u \bar{v} ds,$$

327 which, after using Green's formula for the Laplace-Beltrami operator, can be readily
 328 implemented using the existing finite element mass and stiffness matrices. The for-
 329 mulation for Padé-based ABC is described in [44, Section 1.3.4.3]. The variational
 330 formulation is then discretized with a p -FEM conformal H^1 -basis using integrated
 331 Legendre polynomials [61].

332 **Free field propagation.** For the validation, we consider a radiating point source
 333 in a uniform mean flow located at \mathbf{x}_s , with the mean flow density and speed of
 334 sound set to unity. The exact solution is known through the Prandtl-Lorentz-Glauert
 335 transformation [34]

$$336 \quad u(\mathbf{x}) = \frac{1}{\beta} G(|\mathbf{x}' - \mathbf{x}'_s|, \omega') e^{\frac{ik_0(\mathbf{M} \cdot \boldsymbol{\varphi})}{\beta^2}}, \quad \mathbf{x}' = \mathbf{x} + \frac{(\mathbf{M} \cdot \mathbf{x})}{\beta(1 + \beta)} \mathbf{M}, \quad \omega' = \frac{\omega}{\beta},$$

338 where G is the usual Green kernel of the Helmholtz equation written in transformed
 339 coordinates. We solve the problem in two-dimensions using the finite element library
 340 **GmshFEM** [59]. The computational domain is a disk of unit radius, and the ABC is
 341 applied on the outer circular boundary. A Dirac source is applied at the origin. We
 342 measure the relative L^2 -error with respect to the analytical solution in the restricted
 343 domain $\Omega_{2h} = \Omega \setminus B_{2h}(\mathbf{x}_s)$, where $B_{2h}(\mathbf{x}_s)$ is the ball of radius $2h$ centered at the
 344 origin of the source \mathbf{x}_s , with h the typical mesh size. The mesh is refined by a factor
 345 5 around the point source. The polynomial order p of the shape functions is increased
 346 consistently with the Mach number in order to leverage the pollution effect. We
 347 denote $d_{\lambda} = \frac{2\pi p}{k_0 h} (1 - M)$ the number of points per wavelength, that we fix to $d_{\lambda} = 8$.
 348 Since we deal with a purely propagative problem, there is no evanescent modes hitting
 349 the boundary Γ and we set $\alpha = 0$ for the ABCs.

350 The real part of the solution at $M = 0.95$ is reported in Fig 2.2 as well as the
 351 relative L^2 -error as a function of the Mach number. The flow angle has been fixed to
 352 $\theta = \pi/4$, and we have $M_x = M \cos(\theta)$, $M_y = M \sin(\theta)$. The relative error stays below

353 1% for a Mach number close to 1 using a fourth-order Padé approximation, thanks to
 354 the combination of the high-order discretization basis and absorbing boundary condi-
 355 tion. We have observed very little dependency to θ in our numerical results. A poor
 356 approximation of the square-root operator is only able to deal with low to moderate
 357 Mach numbers. The second order operator $\text{ABC}^{\text{T}1,0}$ provides a reasonably accurate
 358 ABC for moderate Mach numbers at no supplementary numerical cost, which we
 359 keep in mind for domain decomposition. We recall that including additional curva-
 360 ture terms would largely improve the precision of the ABCs, especially at low Mach
 361 number [44].

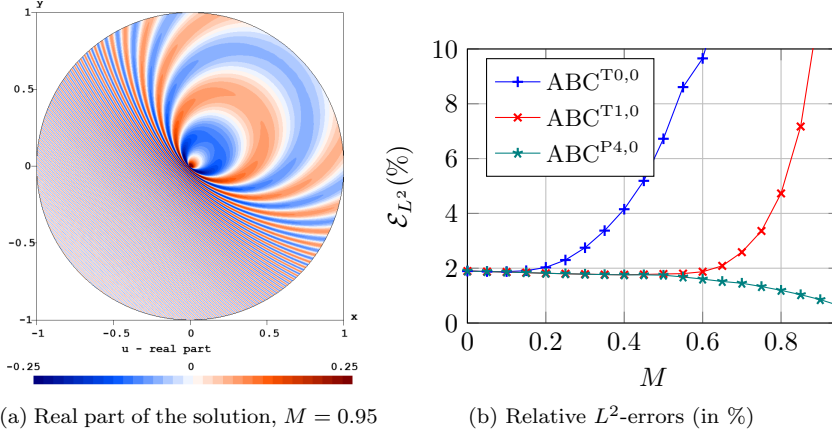


FIG. 2.2. Numerical solution and relative ABC errors with $\alpha = 0$ at $k_0 = 6\pi$ as a function of the Mach number.

3. Optimized Schwarz methods for flow acoustics.

362 **3.1. General framework.** We describe in this section the optimized Schwarz
 363 formulation applied to the Pierce operator. Optimized Schwarz methods are a gen-
 364 eral framework for domain decomposition [27], and can be naturally extended to flow
 365 acoustics as initiated in [39, 68]. We hereafter use the notations and formalism follow-
 366 ing [6, 15]. Let us consider a non-overlapping partition of the computational domain
 367 $\bar{\Omega} = \bigcup_i \bar{\Omega}_i$, $i \in D := \{1, \dots, N_{\text{dom}}\}$, with $\Omega_i \cap \Omega_j = \emptyset$, $i \neq j$. Each surface Γ where a
 368 boundary condition is imposed is decomposed as $\Gamma_i = \Gamma \cap \partial\Omega_i$. For a given subdomain
 369 we denote the indices of connected subdomains by $D_i := \{j \in D; j \neq i; \Sigma_{ji} \neq \emptyset\}$.
 370 For each $j \in D_i$, we define the interface that is shared between two subdomains
 371 $\bar{\Sigma}_{ij} = \bar{\Sigma}_{ji} = \partial\Omega_i \cap \partial\Omega_j$. The outward oriented normal to a subdomain Ω_i , respec-
 372 tively Ω_j , is denoted \mathbf{n}_i , respectively \mathbf{n}_j . The starting point is the Pierce radiation
 373 boundary value problem in each subdomain for the unknown $u_i = u|_{\Omega_i}$
 374

$$(3.1) \quad \begin{cases} -\rho_0 \frac{D}{Dt} \left(\frac{1}{\rho_0^2 c_0^2} \frac{D}{Dt} u_i \right) + \nabla \cdot \left(\frac{1}{\rho_0} \nabla u_i \right) = 0 & \text{in } \Omega_i, \\ \rho_0^{-1} (1 - M_{\mathbf{n}}^2) (\partial_{\mathbf{n}_i} u_i + \mathcal{S}_i u_i) = g_{ij} & \text{on } \Sigma_{ij}, \\ \rho_0^{-1} (1 - M_{\mathbf{n}}^2) (\partial_{\mathbf{n}_i} u_i + \mathcal{L}^+ u_i) = 0 & \text{on } \Gamma_i^\infty. \end{cases}$$

377 where we have set $M_{\mathbf{n}}^2 := M_{\mathbf{n}_i}^2 = M_{\mathbf{n}_j}^2$. The non-reflecting boundary condition on
 378 Γ_i^∞ is imposed through the DtN map \mathcal{L}^+ on Γ_∞ as described in Section 2. The
 379 operator \mathcal{S}_i is the transmission operator, which will be discussed in the next section.
 380 The interfaces unknowns g_{ij} are created locally for each connected subdomain. They

381 are duplicated, including at cross-points, and can be seen as Lagrange multipliers.
 382 The interface coupling is found by eliminating the normal derivatives on a common
 383 interface Σ_{ij} using $\partial_{\mathbf{n}_i} u_i = -\partial_{\mathbf{n}_j} u_i$. We proceed as in the Helmholtz case [15, 67] and
 384 find the surface interface coupling for each subdomain $i \in D$

$$385 \quad (3.2) \quad g_{ij} + g_{ji} = \imath \rho_0^{-1} (1 - M_{\mathbf{n}}^2) (\mathcal{S}_i + \mathcal{S}_j) u_i, \text{ on } \Sigma_{ij}, \forall j \in D_i,$$

387 where \mathcal{S}_j is the transmission operator related to Ω_j . The parallel strategy is performed
 388 following an iterative procedure: each subdomain Ω_i is associated to a computer
 389 process, and computes the next $(n + 1)$ iterate as follows:

- 390 • given the interface data $g_{ij}^{(n)}$, solve the volume problems to get $u_i^{(n+1)}$,
- 391 • update the interface data $g_{ji}^{(n+1)} = -g_{ij}^{(n)} + \imath \rho_0^{-1} (1 - M_{\mathbf{n}}^2) (\mathcal{S}_i + \mathcal{S}_j) u_i^{(n+1)}$.

392 We see that a communication pass is necessary at each iteration, in which each subdo-
 393 main receives the interface data $g_{ij}^{(n)}$ from its connected neighbourhoods and further
 394 sends $g_{ji}^{(n+1)}$. This strategy allows to solve volume problems of small size concurrently
 395 thanks to a direct solver, where the LU factorization is performed only once, and it-
 396 erate on a naturally distributed surface problem. If the iterative method converges,
 397 such a method has the potential to handle large problems at a low memory cost.
 398 The main concern remains to find appropriate transmission operators \mathcal{S}_i and \mathcal{S}_j to
 399 accelerate the convergence of the iterative solver for the interface problem. For that
 400 purpose we take advantage of the ABCs developed in Section 2.

401 **3.2. Choice of transmission operator and convergence factor for the**
 402 **half-space problem.** The convergence factor in the two subdomains case is classi-
 403 cally analyzed by a Fourier analysis [26]. We recall the analysis since it highlights im-
 404 portant properties of our algorithm. Let us focus on the simple half-space setting with
 405 only two subdomains and a uniform mean flow with the density and speed of sound
 406 set to unity. We define the exchange operator \mathcal{T}_{ji} as the exchange of the outgoing
 407 trace leaving Ω_i with the incoming trace coming from Ω_j [55]. We write $g_{ij}^+ = \mathcal{T}_{ji} g_{ji}^-$
 408 in order to highlight when the interface unknown is related to a trace with posi-
 409 tive group velocity (+) or negative group velocity (-), which is especially important
 410 in flow acoustics. For the first exchange operator, we have $g_{ij}^+ = \partial_{\mathbf{n}_i} u_i + \imath \mathcal{S}_i u_i$, with
 411 $\partial_{\mathbf{n}_i} u_i = -\imath \Lambda^+ u_i$, and $g_{ji}^- = -\partial_{\mathbf{n}_j} u_j + \imath \mathcal{S}_i u_j$, that we rewrite as $g_{ji}^- = \partial_{\mathbf{n}_i} u_i + \imath \mathcal{S}_i u_i$. We
 412 then use $\partial_{\mathbf{n}_i} u_i = -\imath \Lambda^- u_i$, since (Λ^+, Λ^-) are respectively the outgoing and incoming
 413 DtN maps on Σ_{ij} following Section 2. We deduce the exchange operators

$$414 \quad \mathcal{T}_{ji} = (\mathcal{S}_i - \Lambda^+) (\mathcal{S}_i - \Lambda^-)^{-1}, \quad \mathcal{T}_{ij} = (\mathcal{S}_j - \Lambda^+) (\mathcal{S}_j - \Lambda^-)^{-1},$$

416 where we have found the second exchange operator from the equality $g_{ji}^+ = \mathcal{T}_{ij} g_{ij}^-$
 417 using the same reasoning. We see that the optimal transmission operator should
 418 be a good approximation of the outgoing DtN map, namely $\Lambda^+ \approx \mathcal{S}_i$ and $\Lambda^- \approx \mathcal{S}_j$.
 419 However we cannot choose $\mathcal{S}_j = \mathcal{S}_i$ as it would select the wrong mean flow orientation,
 420 and break the well-posedness of the subproblems. We choose instead \mathcal{S}_j based on the
 421 flow orientation related to the normal \mathbf{n}_j linked to Ω_j , in order to guarantee that all
 422 subproblems solve the same boundary value problem. This amounts to apply the flow
 423 reversal principle. By imposing a symmetric treatment for the volume subproblems,
 424 we relocate the convection effects on the convergence factor.

425 Let us take a concrete example in two-dimensions and choose $\mathcal{S}_i = \Lambda_1^+$ from
 426 equation (2.8). Assuming $\mathbf{n}_i = (1, 0)$ is the outward normal related to Ω_i , we have
 427 $M_{\mathbf{n}} = M_x$ for \mathcal{S}_i . Since $\mathbf{n}_i = -\mathbf{n}_j$, we use $M_{\mathbf{n}} = -M_x$ for \mathcal{S}_j by reversing the flow.

428 By substitution of the operators into the convergence factor in the partial Fourier
 429 space, we obtain

$$430 \quad \rho(\xi) = \sqrt{|\mathcal{T}_{ji}\mathcal{T}_{ij}|}, \quad \mathcal{T}_{ji}\mathcal{T}_{ij} = \frac{(f_{N,\alpha} - f)(2M_x(-k_0 + M_y\xi) + f_{N,\alpha} - f)}{(f_{N,\alpha} + f)(2M_x(-k_0 + M_y\xi) + f_{N,\alpha} + f)},$$

431

432 where $f = \sqrt{k_0^2 - 2k_0M_y\xi - \beta^2\xi^2}$ is the symbol of the square-root operator and
 433 $f_{N,\alpha} := f_{\{\text{T,P}\}N,\alpha}$ is its Taylor or Padé approximation. In the ideal case, or when
 434 $f_{N,\alpha}$ is close enough to f , the convergence factor is close to zero and the algorithm
 435 converges in two iterations. In domain decomposition the convergence factor ρ acts
 436 on all the Fourier modes ξ . On the contrary to ABCs, it is here of utmost importance
 437 to select $\alpha \neq 0$ in order to capture both the propagative and evanescent parts of the
 438 spectrum. Let us compare in Figure 3.1 the theoretical convergence factor in different
 439 situations. We show the case of a constant mean flow $M = 0.7$ oriented at the angles
 440 $\theta = \{0, \pi/4, \pi/2, \pi\}$ relatively to the straight interface. We refer to the transmission
 441 operators as $\mathcal{S}^{\text{TN},\alpha}$ and $\mathcal{S}^{\text{PN},\alpha}$ following the convention given for the ABCs in Section
 442 2.4. We show the performance of different transmission operators: the Després condi-
 443 tion $\mathcal{S}^{\text{T}0,0}$, the second order Taylor condition $\mathcal{S}^{\text{T}1,\alpha}$ with $\alpha = \{-\pi/2, -\pi/4\}$ and the
 444 Padé condition $\mathcal{S}^{\text{P}4,\alpha}$ with $N = 4$ and $\alpha = \{-\pi/2, -\pi/4\}$.

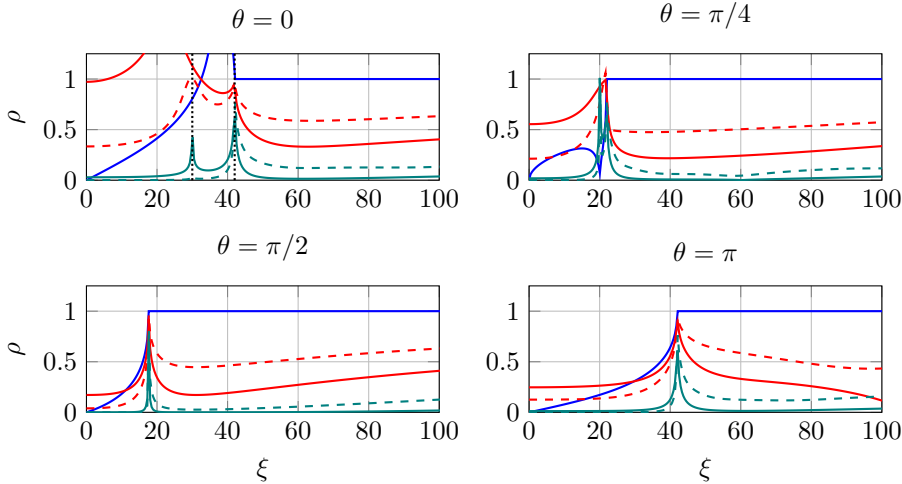


FIG. 3.1. Convergence factor for the half-space problem for different mean flow angles at $M = 0.7$ and $k_0 = 30$. Legend: $\mathcal{S}^{\text{T}0,0}$ (—), $\mathcal{S}^{\text{T}1,-\pi/2}$ (—), $\mathcal{S}^{\text{T}1,-\pi/4}$ (---), $\mathcal{S}^{\text{P}4,-\pi/2}$ (—), $\mathcal{S}^{\text{P}4,-\pi/4}$ (---).

445 The cases $\theta = \{0, \pi\}$ correspond to a flow oriented respectively along the positive
 446 and negative x -direction, such that $M_y = 0$. At $\theta = 0$ inverse upstream modes are
 447 present in the range $\xi \in [k_0, k_0/\beta]$. The square-root approximation is not valid at the
 448 two extreme values, corresponding to grazing waves, resulting in two peaks at $\xi = k_0$
 449 and $\xi = k_0/\beta$ that are delimited by black lines in Figure 3.1. The convergence factor
 450 is deteriorated in this regime for all our transmission operators.

451 The inverse upstream regime still exists at $\theta = \pi/4$ since $M_x > 0$, but is of
 452 shorter range. When $M_x \leq 0$ the convergence factor is smaller than for $M_x > 0$,
 453 for which we observe a similar behaviour to the Helmholtz case [15]. The second
 454 order Taylor approximation with $\alpha = -\pi/2$ provides the best trade-off between the

455 attenuation of propagative and evanescent modes. It is an interesting operator since
 456 no additional cost is required for its implementation. In the Helmholtz case it shows
 457 very close performance to the second order optimized condition O02 [26]. For the
 458 half-space problem, Padé-based transmission operators reach arbitrary precision away
 459 from grazing modes.

460 **3.3. A quasi-optimal algorithm for simple partitions.** The optimized Schwarz
 461 algorithm is implemented in `GmshDDM`, a lightweight domain decomposition library
 462 written in `C++` built on top of the finite element library `GmshFEM` [59], which is itself
 463 based on `Gmsh` [29]. Many flow acoustics benchmarks are freely available for testing.
 464 We here highlight the performance of the transmission operators on academic exam-
 465 ples, and refer to Section 4 for more details regarding its usage in a HPC context.
 466 Regarding the iterative procedure, we compute at each iteration the absolute and
 467 relative residual of the interface problem. We set our convergence criterion to a rela-
 468 tive residual of $r_I = 10^{-6}$. When the exact solution of the problem is not available,
 469 we compute the relative L^2 -error with a usual finite element computation without
 470 domain decomposition, referred to as relative mono-domain L^2 -error. In each case we
 471 verify that the interface residual is of same order of magnitude as the mono-domain
 472 error.

473 **Guided propagation in uniform mean flow.** Let us consider a multi-modal
 474 acoustic propagation in a straight waveguide geometry in a uniform mean flow only
 475 oriented along the x -direction, that is $M_y = 0$. The waveguide is a rectangular
 476 geometry of size $[0, L] \times [0, H]$ with $L = 1$ and $H = 0.5$. It is decomposed into equally
 477 spaced subdomains separated by straight interfaces at fixed x -positions. We use a
 478 superposition of the 30 first transverse modes of unit amplitude as input boundary
 479 condition at $\{x = 0\}$. A perfectly matched layer (PML) is set as output boundary
 480 condition at $\{x = L\}$. For the moment we perform the partitioning such that the
 481 interfaces do not pass through the PML. Homogeneous Neumann boundary conditions
 482 are set on the upper and lower waveguide walls. The exact solution is available by
 483 modal superposition.

484 The problem is discretized using quadrilateral elements of typical size h and a
 485 p -FEM basis. We use $d_\lambda = 12$ according to the definition provided in Section 2.5. We
 486 report in Table 3.1 the number of GMRES and Jacobi iterations to reach an interface
 487 residual of $r_I = 10^{-6}$.

TABLE 3.1

Number of GMRES (Jacobi) iterations at $M_x = -0.7$ (left) and $M_x = 0.7$ (right) when changing the number of subdomains. Simulation parameters: $d_\lambda = 12, p = 4, k_0 = 30$ (dnc: did not converge).

N_{dom}	$\mathcal{S}^{\text{T0},0}$	$\mathcal{S}^{\text{T1},-\pi/4}$	$\mathcal{S}^{\text{P8},-\pi/4}$	N_{dom}	$\mathcal{S}^{\text{T0},0}$	$\mathcal{S}^{\text{T1},-\pi/4}$	$\mathcal{S}^{\text{P8},-\pi/4}$
4	28 (dnc)	19 (20)	3 (3)	4	49 (dnc)	45 (dnc)	3 (3)
8	61 (dnc)	43 (117)	7 (7)	8	117 (dnc)	97 (dnc)	7 (7)
16	155 (dnc)	87 (dnc)	15 (15)	16	268 (dnc)	197 (dnc)	17 (45)

488 We observe that convergence is harder to achieve when $M_x > 0$ due to inverse
 489 upstream modes, in particular when M_x is large. The Padé conditions are very
 490 effective in this case since they can approximate the exact DtN map up to arbitrary
 491 precision on a straight interface. We observe indeed convergence in N_{dom} iterations
 492 with a Jacobi solver. The GMRES solver accelerates the convergence of the algorithm
 493 even if some transmission conditions do not converge with the Jacobi solver.

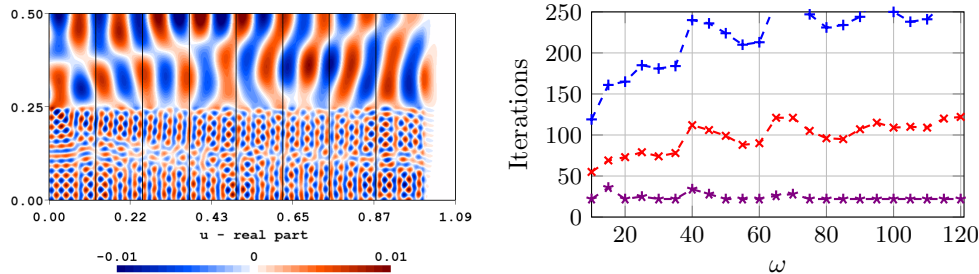
494 **Guided propagation without flow in a layered media.** For the second
 495 example we point out that the transmission operators are also suitable for a class of
 496 problems with variable coefficients, according to the ABC performance conducted in
 497 [45]. We select a normalized layered mean density and speed of sound

$$498 \quad \rho_0(y) = \begin{cases} 1.25, & y \in [0, H/2] \\ 0.5, & y \in [H/2, H] \end{cases}, \quad c_0(y) = \begin{cases} 0.5, & y \in [0, H/2] \\ 2, & y \in [H/2, H] \end{cases}.$$

500 Such a situation is encountered for turbofan exhaust acoustic radiation, see Section
 501 4. The input is the cosine function $u_{\text{in}}(y) = \cos(2\pi y/H)$, and the duct is terminated
 502 again by a PML that approximates the outgoing solution, which is validated using a
 503 mode-by-mode analysis. The key to achieve rapid convergence is to correctly localize
 504 the square-root operator. We follow an idea used in one-way modeling [42], which
 505 consists in expressing equation (2.3) as follows

$$506 \quad (3.3) \quad \Lambda^+ = \omega \sqrt{1 + \mathcal{Z}}, \quad \mathcal{Z} = (c_0^{-2} - 1) + \nabla_{\Gamma}(\rho_0^{-1} \nabla_{\Gamma})/\omega^2,$$

508 for which we further apply the branch-cut rotation technique from Section (2.4).
 509 This operator encodes the exact DtN map for the half-space problem, and results
 510 in a correct clustering of the eigenvalues [44]. We report in Figure 3.2 the number
 511 of iterations as a function of the angular frequency to achieve convergence up to
 512 $r_I = 10^{-6}$ for various transmission operators. Since we do not have an exact solution
 513 for this problem the convergence is verified by computing the relative mono-domain
 514 L^2 -error.



(a) Real part of the solution at $\omega = 120$.
 Black lines delimit the subdomains.

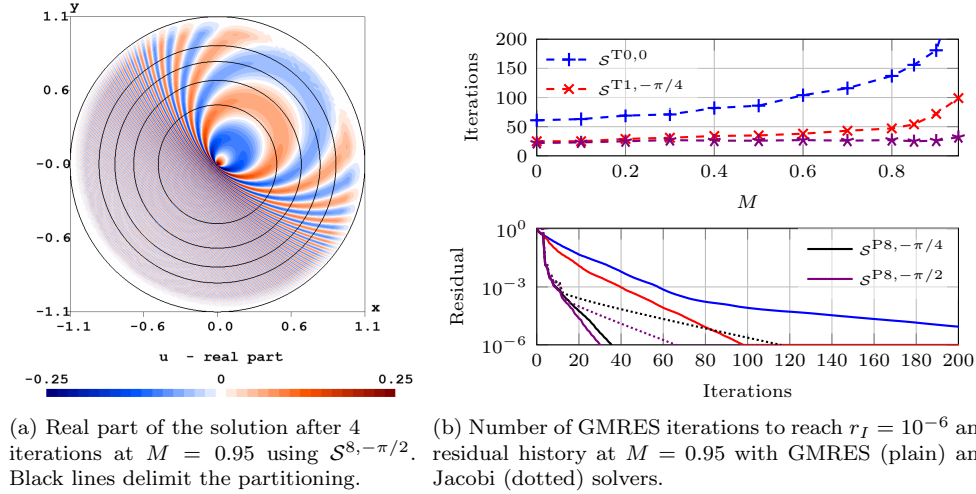
(b) Number of GMRES iterations to reach $r_I = 10^{-6}$.

FIG. 3.2. Converged numerical solution and iteration count when varying ω for the operators $\mathcal{S}^{T0,0}$ (-+-), $\mathcal{S}^{T1,-\pi/4}$ (-*-*) and $\mathcal{S}^{P8,-\pi/4}$ (-*-). Simulation parameters: $N_{\text{dom}} = 8, d_{\lambda} = 12, p = 4$.

515 With the Padé transmission operator, we observe that the number of iterations
 516 is close to the number of subdomains, which suggests that we have found the block
 517 LU factorization at the continuous level. The relative mono-domain L^2 -error indeed
 518 reaches $10^{-3}\%$ after N_{dom} iterations, even with a Jacobi solver. The second order
 519 Taylor condition gives reasonable results. Fewer iterations are required when the
 520 second order transmission operator is used under the form (3.3).

521 **Free field propagation.** The last academic example is the point source radi-
 522 ation problem considered in Section 2.5. We split the domain into concentric disks
 523 of equal area, such as there are no cross-points, see Figure 3.3. We discuss the case
 524 of arbitrary partitioning in Section 4.1. We use again a PML as outgoing boundary

525 condition. The mesh is refined by a factor 5 around the point source. As in Section
 526 2.5 the shape functions polynomial order is increased steadily with the Mach number.
 527 The mesh density is fixed to $d_\lambda = 8$ for the shortest wavelength.



(a) Real part of the solution after 4 iterations at $M = 0.95$ using $\mathcal{S}^{8,-\pi/2}$. Black lines delimit the partitioning. (b) Number of GMRES iterations to reach $r_I = 10^{-6}$ and residual history at $M = 0.95$ with GMRES (plain) and Jacobi (dotted) solvers.

FIG. 3.3. Numerical solution, iteration count as a function of the Mach number, and residual history for various transmission operators. Simulation parameters: $k_0 = 6\pi$, $\theta = \pi/4$, $d_\lambda = 8$, $N_{\text{dom}} = 5$.

528 Figure 3.3 shows the real part of the solution after the fourth GMRES iteration for
 529 the condition $\mathcal{S}^{P8,-\pi/2}$ with $N_{\text{dom}} = 5$ at $M = 0.95$, $\theta = \pi/4$. We immediately see the
 530 good accuracy of the numerical solution after a single forward sweep. The averaged
 531 relative L^2 -error with the exact solution is 1.8%, which is also the precision reached
 532 by the PML. We report the residual history for different transmission operators, and
 533 analyze the evolution of the number of iterations when varying the Mach number.
 534 The Padé condition shows a very fast convergence during the first iterations even
 535 with a Jacobi solver. The convergence is then slowed down due to the presence of
 536 evanescent modes on the interfaces. Using $\alpha = -\pi/2$ instead of $\alpha = -\pi/4$ indeed
 537 accelerates the speed of convergence. While the convergence of low order operators
 538 deteriorates at high Mach numbers when $M > 0.8$, Padé conditions are more robust
 539 and can almost maintain a constant number of iterations up to $M = 0.95$. Further
 540 tests show that Padé conditions are little sensitive to d_λ and k_0 , as observed in the
 541 Helmholtz case [15].

542 **Conclusion.** In this section we have analyzed the convergence of the optimized
 543 Schwarz method for a class of academic problems with strong convection and variable
 544 coefficients. The proposed transmission operators perform well for unbounded wave-
 545 guide and free field problems, where we have found quasi-optimal local operators in the
 546 spirit of [19, 47]. In particular, the second order Taylor operator is interesting for its
 547 low computational cost and straightforward implementation, albeit more iterations.

548 **4. Industrial applications and high-performance computing.** We now ad-
 549 dress the development and application of the domain decomposition method in an
 550 industrial context, with the final aim to solve large scale problems on a distributed
 551 multi-core architecture. We recall that the available computer memory is the main
 552 bottleneck preventing the simulation of high frequency problems in the industry. We

553 first explain how to adapt the domain decomposition methodology to industrial prob-
 554 lems. We then briefly present two industrial benchmarks and assess the parallel
 555 scalability of our solver.

556 **4.1. A robust domain decomposition methodology.** We have seen in the
 557 previous sections that the domain decomposition algorithm could be quasi-optimal for
 558 relatively simple partition boundaries shapes. For industrial cases we must however
 559 find a systematic way to partition a given computational domain, that might be
 560 already meshed, while ensuring a good load balancing of the subproblems unknowns.
 561 We resort to the automatic graph partitioner METIS [36] for the generation of the
 562 subdomains, allowing a fully automatic method. It is set to minimize the size of the
 563 interface problem, and has a connectivity graph of $\mathcal{O}(N^{1/d})$ in d dimension, which
 564 drives the communication speed between subdomains. While the approach is very
 565 attractive at the industrial level, it also has drawbacks that affects the convergence of
 566 the iterative method. The first one is the presence of cross-points. Cross-points are a
 567 well-known theoretical and numerical issue for domain decomposition methods, and
 568 is an active topic of research [16, 18]. By construction of our method, we duplicate all
 569 the interface unknowns at the cross-points and do not apply any treatment on them.
 570 In practice it has the effect to slow down the convergence of the iterative solver.
 571 The second issue is non-smooth interface boundaries: using an automatic partitioner
 572 generates broken line interfaces, which deteriorates the quality of our transmission
 573 operators that are developed for smooth interfaces. Note that the interfaces are now
 574 cutting through the PMLs. Evanescent modes will propagate in these layers, and are
 575 naturally taken into account in our transmission conditions. The convergence to the
 576 mono-domain solution is still ensured, see also [50].

577 In order to see how such a partitioning impacts the iterative method, we reproduce
 578 in Figure 4.1 the free field propagation case from Figure 3.3 but using an arbitrary
 579 partitioning. We observe that the transmission operators still converge reasonably
 580 well, but that the Padé based conditions loose robustness with respect to the Mach
 581 number, frequency and mesh size. The second order Taylor condition here converges
 582 in a comparable number of iterations as the Padé condition. The former is hence
 583 more efficient since it has a lower computational cost, and is also easier to implement.
 584 The choice $\alpha = -\pi/2$ seems to be the best trade-off in such situations, where the
 585 high-order evanescent modes living on the interfaces dominate the overall error for
 586 small values of the interface residual.

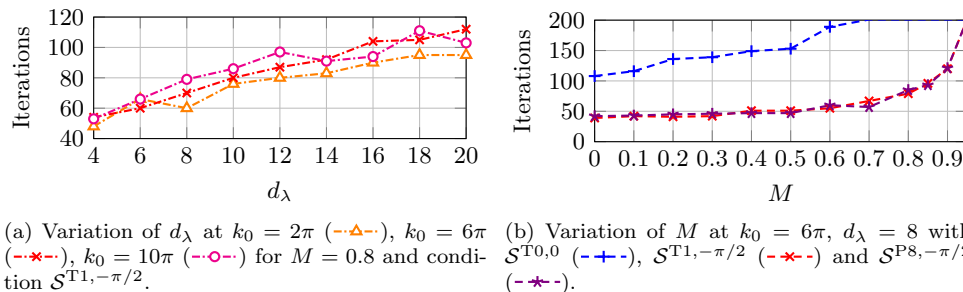


FIG. 4.1. Number of GMRES iterations to reach $r_I = 10^{-6}$ for the point source free field problem with arbitrary partitioning and $N_{dom} = 16$.

587 In such a case the theoretical analysis is more difficult, and we view the transmis-

588 sion operators as a preconditioner for the interface problem. The same observations
 589 hold in 3D, with a stronger dependency of the number of iterations with respect to
 590 the parameters k_0 , d_λ and M .

591 To summarize, we improve the robustness of our approach at the price of com-
 592 plicated interface geometries, where quasi-optimal transmission conditions are much
 593 harder to design. Nevertheless, second-order conditions perform reasonably well in
 594 this context, and we will use the transmission operator $\mathcal{S}^{T1, -\pi/2}$ in the rest of the
 595 article.

596 4.2. Aeroengine intake and exhaust acoustic radiation benchmarks.

597 Engine noise is one of the most important acoustic source from modern commercial
 598 aircraft. On modern high by-pass ratio engines, sound is radiated by the inlet fan,
 599 by-pass duct and hot jet exhaust. These source of noise must be reduced especially
 600 during landing and take-off for health and environmental purposes.

601 The Pierce operator has recently been advocated to simulate such problems [62],
 602 which has been shown to be a reasonable alternative to the Linearized Euler Equations
 603 especially in the high frequency regime [37]. A preliminary step is to compute a steady
 604 mean flow for a given flight configuration, which is performed by an external solver.
 605 We consider the approach and sideline configurations, representing respectively the
 606 landing and take-off flight phases, to simulate respectively the sound propagating in
 607 a hot jet exhaust and turbofan intake. For the intake problem [25], a compressible,
 608 potential mean flow is solved from a non-linear Poisson problem [28]. The computed
 609 flow presents smooth variations but shows a strong Mach number reaching values up
 610 to $M \approx 0.8$ in the throat of the nacelle, see Figure 4.2a. For the exhaust problem
 611 [32], a Reynolds-averaged Navier–Stokes (RANS) simulation was run. The mean flow
 612 is no more potential due to the mixing of the cold and hot jets. The Mach number
 613 shown in Figure 4.2b is moderate but the mean speed of sound and density exhibit
 614 strong variations, taking the form of a layered profile as presented in Figure 3.2. In
 615 order to avoid acoustic instabilities the mean flow boundary layer is removed as a
 616 pre-processing step [71]. Finally the pre-computed quantities c_0 , ρ_0 , \mathbf{v}_0 are mapped
 617 on the acoustic mesh using a simple linear interpolation.

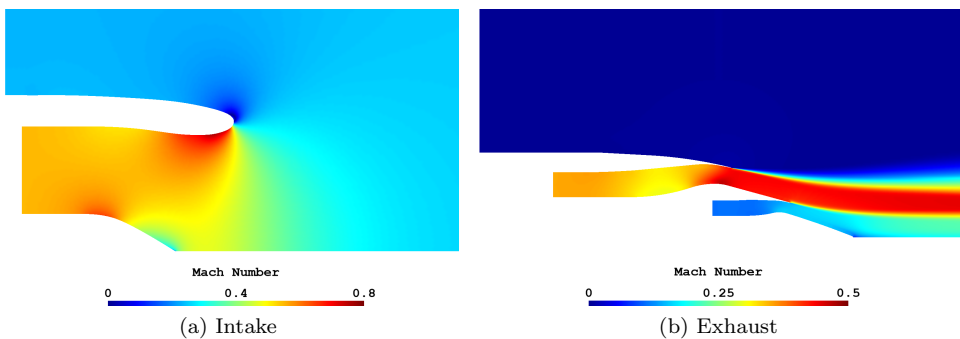


FIG. 4.2. Mach number in the xy -plane for the intake problem at sideline configuration and exhaust problem at approach configuration

618 For a given mean flow, the Pierce boundary value problem can be set up. For
 619 the turbofan intake problem, tonal noise is generated at multiples of the so-called
 620 blade passing frequency (bpf). A fixed annular duct mode of azimuthal and radial
 621 orders (m, n) is used to model the acoustic source on the fan face surface. The

622 modal order to be used at the bpf is given by the number of fan blades following
 623 the Tyler-Sofrin analogy [69]. An acoustic lining treatment is set on the walls of the
 624 nacelle duct. It models the acoustic absorption of a micro perforated plate panel
 625 backed by an air cavity, and is described by a complex-valued acoustic impedance
 626 $\mathcal{Z}(\omega)$. The impedance is described by the Ingard-Myers boundary condition [52], and
 627 implemented following [24, 37]. In practice the acoustic liner has the effect to broaden
 628 the acoustic spectrum and creates back-reflected waves [58]. Finally a cylindrical
 629 version of the perfectly matched layer [46] truncates the exterior domain. A PML is
 630 also used for the input boundary condition in order to both impose the annular mode
 631 and absorb back-reflected waves.

632 For the exhaust problem we impose a plane wave in the heated core jet, using again
 633 a PML on the reflected field. A cylindrical version of the PML truncates the exterior
 634 domain. Both benchmarks have been validated in a two-dimensional, axi-symmetric
 635 setting, which are used for a qualitative comparison with the three-dimensional cases.
 636 We refer to [25] and [35, 66] for more details on the benchmarks and their applications.

637 **4.3. Solving large scale problems.** In this last section we discuss the scala-
 638 bility of our solver and illustrate its capability on high frequency problems.

639 **Parallel algorithm and scalability.** Let us describe the parallel procedure used
 640 in our domain decomposition library `GmshDDM`. All the computations are performed
 641 in double-precision. The high-level algorithm is summarized in Algorithm 4.1. We
 642 assign one subdomain to a computer process, and use multi-threading per subdomain.
 643 After the assembly, the LU factorization is performed once by `MUMPS` [2], where we use
 644 the default sparse solver. We enter the iterative solver where we rely on the `PETSc`
 645 `GMRES` implementation. We have modified the matrix-vector product thanks to a
 646 matrix free `PETSc` shell [8]. In our custom matrix-vector product we i) receive and
 647 send at each iteration the local interface unknowns g_{ij} to the connected subdomains
 648 using asynchronous MPI communication, and ii) solve the subdomains volume and
 649 surface problems using the initial LU factorization.

Algorithm 4.1 Domain decomposition algorithm for the subdomain Ω_i

1. **Initialization:** read mesh and interpolate mean flow
 2. **Assembly:** assemble the finite element matrix with `GmshFEM`,
 3. **Factorization:** call `MUMPS` and run a sparse LU decomposition for the volume subproblem,
 4. **Surface Assembly:** assemble the surface interface problem,
 5. **Iterative solver:** enter `GMRES` for the interface problem. At each iteration do until convergence:
 - (a) receive g_{ij} and send the updated data g_{ji} to the connected subdomains,
 - (b) compute the local matrix-vector product,
 6. **Post-processing**
-

650 We have measured the weak scalability of our solver for a fixed number of itera-
 651 tions, and a problem size of roughly 800 000 unknowns per subdomain. We observed
 652 80% scalability up to 1024 MPI processes for a total of 16 384 cores. One of the scala-
 653 bility limitation is the load balancing of the unknowns by the graph partitioner. With
 654 1024 subdomains we observed a 40% relative memory increase in the peak memory
 655 usage over all the processes.

656 For a small number of large subdomains, the computational most intensive task is
 657 the time and memory used for the LU factorization, which scales as $\mathcal{O}(m^2 N)$ with m
 658 the bandwidth of the matrix and N its size. On the contrary, with a large number of

659 small subdomains the most computational intensive task is the iterative solver, since
 660 the number of iterations scales as $\mathcal{O}(N_{\text{dom}}^{1/3})$ in 3D. However the memory footprint of
 661 the iterative solver is low since it acts on a lower dimensional problem. An efficient
 662 computation relies on a trade-off between the total number of subdomains and the
 663 size of each subdomain, which is driven by the available computational resources.

664 **A high frequency solver.** We first solve a small and moderate size problem
 665 for respectively the intake and exhaust benchmarks, containing respectively around
 666 25 and 50 wavelengths in the domain. The total problem size is respectively 10 and
 667 86 millions of unknowns using basis functions of polynomial order $p = 4$, see Table
 4.1. The intake case is solved at the first blade passing frequency $f = 1300$ Hz for

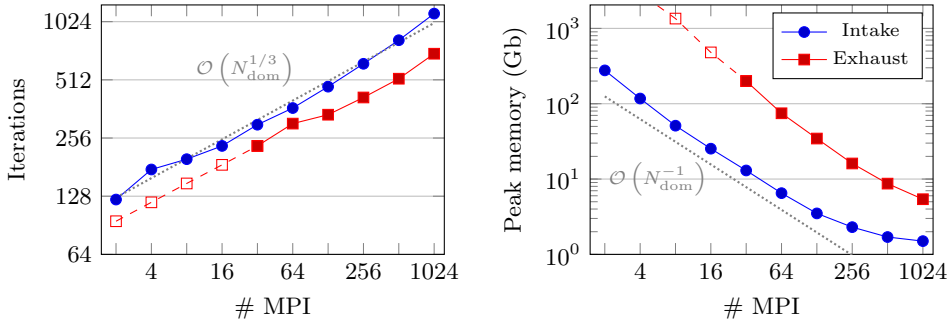
TABLE 4.1

Total problem size for the intake and exhaust problems used for the strong scalability assessment. The p -FEM order is set to 4. nnz: number of non-zeros entries.

	Frequency [Hz]	unknowns	nnz	memory (est.)	tetra
Intake	1300	10M	730M	740Gb	890k
Exhaust	2×7497	86M	6.3B	≈ 10 Tb	7.7M

668

669 the annular mode $(24, 0)$ imposed on the fan face, and the exhaust is solved at the
 670 frequency $f = 2 \times 7497$ Hz for the plane wave mode $(0, 0)$ imposed at the end of the
 671 heated core duct. We solve both problems and vary the number of MPI processes.
 672 The number of iterations and maximum peak memory usage over the MPI processes
 673 are reported in Figure 4.3. We have added estimations for the exhaust problem
 674 when computational resources were too much demanding, in particular the memory
 675 estimation was performed during the MUMPS analysis phase. A direct solver for the
 676 exhaust problem would require around 10 Tb of memory for an in-core factorization.



(a) Number of GMRES iterations to reach a relative residual of $r_T = 10^{-6}$.

(b) Peak memory usage over all processes

FIG. 4.3. Strong scalability assessment. Iteration count and peak memory usage for the intake problem at 1300 Hz, and exhaust problem at 2×7497 Hz. Dashed lines are estimated data.

677 For a low number of MPI processes, we observe a superlinear scaling in terms of
 678 computational time and memory, since the most demanding task is the LU factoriza-
 679 tion. For example the exhaust problem was solved in 7 minutes with 256 MPIs with
 680 a peak memory usage of 16.1 Gb per process, highlighting the speed and low-memory
 681 footprint of the method. Beyond a certain number of subdomains the volume sub-
 682 problems are too small and there is no further gain from domain decomposition, which

683 can be noticed from the peak memory consumption in Figure 4.3b. The peak memory
 684 becomes bounded by the pre-processing and assembly phases, and the solving time is
 685 bounded by the iterative solver. Note that with 1024 MPIs the interface problem for
 686 the exhaust case totalizes 12 millions unknowns, but a memory footprint of less than
 687 1 Gb and a timing of 0.4 seconds per iteration on eight CPU threads.

688 We continue and attempt to solve larger size problems. We set the intake problem
 689 at 5 times the blade passing frequency, $f = 6500$ Hz, for the input mode $(48, 0)$ using
 690 basis functions of order $p = 6$, corresponding to a three-dimensional simulation of
 691 roughly $125 \times 100 \times 100$ wavelengths in the computational domain. We split the domain
 692 into 1024 subdomains, such that each subdomain contains approximately one million
 693 unknowns. The global mesh is composed of 30 millions tetrahedra. The problem size
 694 and timing are shown in Table 4.2. The algorithm converged to a relative residual of
 695 $r_I = 10^{-4}$ in 1293 iterations for a total solving time of 3 hours and 48 minutes. Note
 696 that the large input frequency increases the number of GMRES iterations because of
 697 the strong indefiniteness of the problem. The real part of the solution is shown in
 698 Figure 4.4. Strong variations of the wavelength can be observed in the throat of the
 699 nacelle.

TABLE 4.2
 Total problem size and computational data for the intake problem at 5 bpf ($f = 6500$ Hz)

Cores (MPI×threads)	unknowns	nnz	peak memory	pre-pro	GMRES	It
1024×20	1.1B	167B	70Gb	24min	3h24min	1293

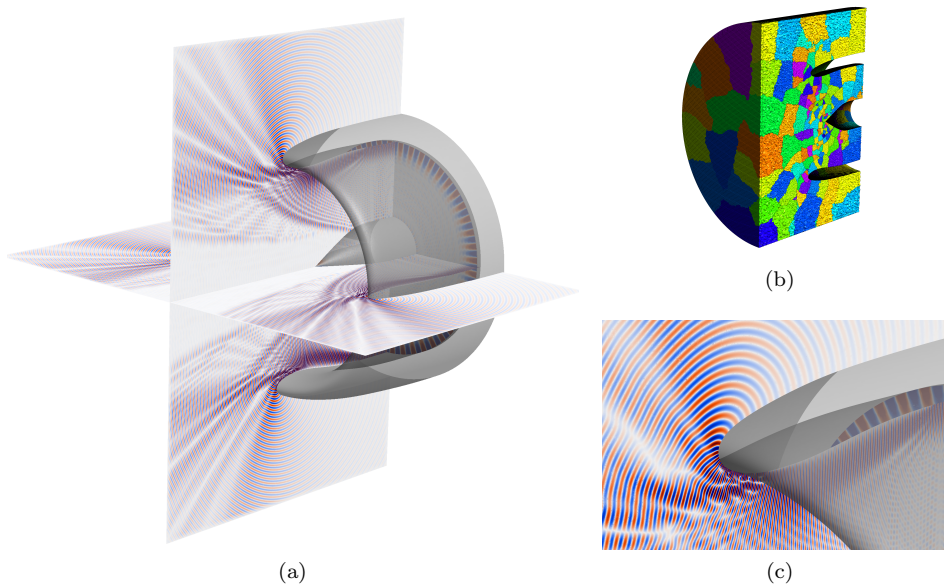


FIG. 4.4. Real part of the solution at 5 bpf (6500 Hz), cut view of the meshed partitions, and zoom in the throat of the nacelle

700 We also solve the exhaust benchmark set at the input frequency $f = 40$ kHz with
 701 basis function of order $p = 4$. The mesh is composed of 122 millions tetrahedra, and
 702 the shortest wavelength is discretized with approximately 6.7 degrees of freedom. The

703 computational domain is partitioned into 4096 subdomains, each containing approxi-
 704 mately 320 000 unknowns. The algorithm reached a relative residual of $r_I = 10^{-4}$ in
 705 15 minutes and 555 iterations, see Table 4.3. The real part of the solution is shown in
 706 Figure 4.5. We observe guided propagation and a shortening of the wavelength in the
 707 bypass duct, as well as the wave refraction through the shear layer that impacts the
 708 acoustic radiation in the far field. As for the intake problem, we observed convergence
 709 slowdowns when increasing the input frequency, in particular for small values of the
 710 relative residual.

711 We ran the exhaust benchmark with 4096 MPIs for the frequencies 20, 30, 40
 712 and 50 kHz. All reached a relative residual of $r_I = 10^{-4}$ within 1000 iterations, but
 713 required respectively 1400, 3400, 6600 and 7500 GMRES iterations to reach $r_I =$
 714 10^{-6} . Future research should investigate the introduction of a suitable coarse space
 715 to precondition the global interface problem. It could rely on interfaces plane waves
 [56], two-level methods [14], or a high-frequency solver for the eikonal equation.

TABLE 4.3
 Total problem size and computational data for the exhaust problem at $f = 40$ kHz.

Cores (MPI×threads)	unknowns	nnz	peak memory	pre-pro	GMRES	It
4096×16	1.3B	96B	18.4Gb	1min	14min	555

716

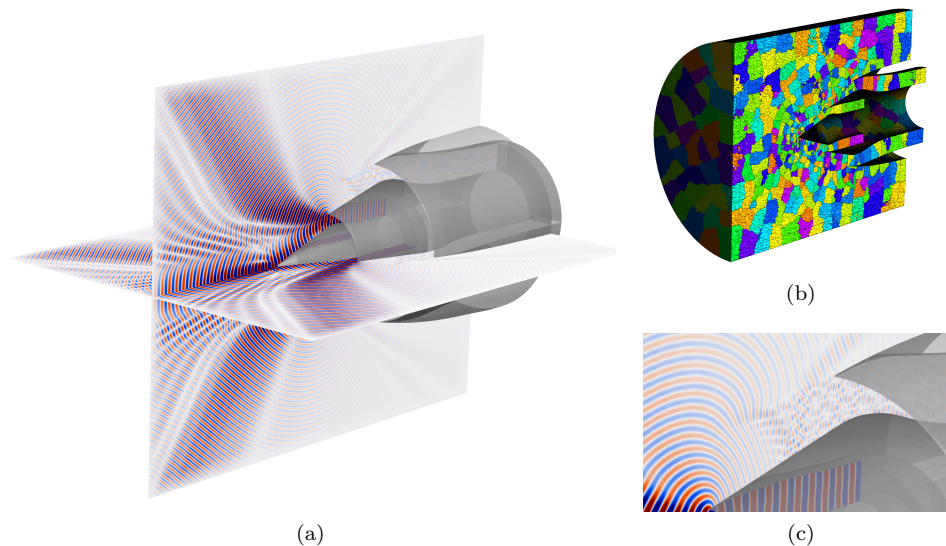


FIG. 4.5. Real part of the solution at 40 kHz, cut view of the meshed partitions, and zoom in the bypass duct.

717 **5. Conclusion and perspectives.** We have presented a hybrid direct-iterative
 718 distributed memory solver for realistic time-harmonic flow acoustic problems governed
 719 by the Pierce operator. Our solver is based on a non-overlapping optimized Schwarz
 720 method which is suitable for large scale high frequency problems that would require
 721 too much memory for direct solvers. The method is fully automatic and scales up
 722 to thousands of MPI processes, allowing to solve problems with more than a billion
 723 of high-order unknowns. These achievements were possible thanks to theoretical and

724 computational contributions. On the one hand, we designed ABCs that are robust
 725 at Mach numbers close to 1 on arbitrary convex boundary shape. This led us to
 726 propose suitable transmission operators for a class of open problems with strong non-
 727 uniform mean flows. On the other hand, a high-performance framework for domain
 728 decomposition has been developed in the `GmshDDM` software, allowing an easy setting of
 729 industrial problems. Many improvements are already possible. At the solver level one
 730 may add p -order adaptivity, solve the interface problem on GPUs and use Block-Low
 731 Rank factorization for the subproblems. Regarding convergence, the use of overlap
 732 and PML-based transmission operator could be beneficial. A coarse space should be
 733 investigated to improve the scalability of the iterative solver. A promising perspective
 734 is to partition the computational domain with straight partitions directly through
 735 the computational mesh, and embed transmission operators as immersed boundaries.
 736 This could be coupled with advanced discretization methods such as the hybrid high-
 737 order, hybridisable discontinuous Galerkin or wave-based Trefftz methods.

738 Finally, let us mention that domain decomposition methods are strongly linked to
 739 the physics of the problem, which makes this class of methods less robust than direct
 740 solvers. In addition domain decomposition methods require more investigations to
 741 efficiently address multiple right-hand-side.

742 **Appendix A. Formal factorization of the Pierce operator.** We present
 743 the calculations leading to the system for the operator equation (2.4). The factoriza-
 744 tion (2.1) is expanded as

$$745 \quad (A.1) \quad \mathcal{P}^* u = \partial_x^2 + \imath (\Lambda^+ + \Lambda^-) \partial_x + \imath \text{Op} \{ \partial_x \lambda^+ \} - \Lambda^- \Lambda^+ + \mathcal{R},$$

747 $\mathcal{R} \in \text{OPS}^{-\infty}$. We then develop the Pierce operator as

$$748 \quad \mathcal{P} = -\frac{1}{\rho_0 c_0^2} \frac{D^2}{Dt^2} - \rho_0 \left(\mathbf{v}_0 \cdot \nabla \left(\frac{1}{\rho_0^2 c_0^2} \right) \right) \frac{D}{Dt} + \nabla \cdot \left(\frac{1}{\rho_0} \nabla \right),$$

750 and expand the double material derivative as follows

$$751 \quad \frac{D^2}{Dt^2} = -\omega^2 + 2\imath\omega \mathbf{v}_0 \cdot \nabla + \mathbf{v}_0 \cdot \left((\mathbf{v}_0^T \mathbb{H})^T + \partial \mathbb{V}_0 \nabla \right),$$

$$752 \quad \mathbb{H} = \begin{pmatrix} \partial_x^2 & \partial_{xy}^2 & \partial_{xz}^2 \\ \partial_{yx}^2 & \partial_y^2 & \partial_{yz}^2 \\ \partial_{zx}^2 & \partial_{zy}^2 & \partial_z^2 \end{pmatrix}, \quad \partial \mathbb{V}_0 = \begin{pmatrix} \partial_x(v_x) & \partial_x(v_y) & \partial_x(v_z) \\ \partial_y(v_x) & \partial_y(v_y) & \partial_y(v_z) \\ \partial_z(v_x) & \partial_z(v_y) & \partial_z(v_z) \end{pmatrix},$$

754 where \mathbb{H} is the Hessian matrix that applies to a wavefield u , and $\mathbf{v}_0 = (v_x, v_y, v_z)^T$. In
 755 that way we are able to isolate the contribution coming from the x -derivative, which is
 756 the normal derivative in a half-space setting. By identification of the first and zeroth
 757 order normal derivatives with (A.1), we form the system

$$758 \quad \begin{cases} \imath (\Lambda^+ + \Lambda^-) = \frac{1}{1-M_x^2} (\mathcal{A}_1 + \mathcal{A}_0) \\ \imath \text{Op} \{ \partial_x \lambda^+ \} - \Lambda^- \Lambda^+ = \frac{1}{1-M_x^2} (\mathcal{B}_2 + \mathcal{B}_1) \end{cases},$$

759

760 with the differential operators

$$\begin{aligned}
 761 \quad \mathcal{A}_1 &= -2ik_0M_x - 2M_x(M_y\partial_y + M_z\partial_z), \\
 762 \quad \mathcal{A}_0 &= -\frac{v_0}{c_0^2} \cdot (\nabla(v_x) + \rho_0^2\nabla(\rho_0^{-2}c_0^{-2})v_x) + \rho_0\partial_x(\rho_0^{-1}), \\
 763 \quad \mathcal{B}_2 &= k_0^2 - 2ik_0(M_y\partial_y + M_z\partial_z) + (1 - M_y^2)\partial_y^2 + (1 - M_z^2)\partial_z^2, \\
 764 \quad \mathcal{B}_1 &= -\frac{v_0}{c_0^2} \cdot [\nabla(v_y)\partial_y + \nabla(v_z)\partial_z + \rho_0^2\nabla(\rho_0^{-2}c_0^{-2})(v_y\partial_y + v_z\partial_z + i\omega)] \\
 765 \quad &+ \rho_0\partial_y(\rho_0^{-1})\partial_y + \rho_0\partial_z(\rho_0^{-1})\partial_z,
 \end{aligned}$$

767 where we recall $k_0 = \omega/c_0$. Each operator is indexed by its degree of homogeneity
 768 with respect to $(\omega, \partial_y, \partial_z)$. Finally we eliminate Λ^- from the system and obtain the
 769 operator equation

$$770 \quad (1 - M_x^2)((\Lambda^+)^2 + i\text{Op}\{\partial_x\lambda^+\}) + i(\mathcal{A}_1 + \mathcal{A}_0)(\Lambda^+) = (\mathcal{B}_2 + \mathcal{B}_1).$$

772 We can readily find Λ^- through

$$773 \quad \Lambda^- = -i\frac{1}{1 - M_x^2}(\mathcal{A}_1 + \mathcal{A}_0) - \Lambda^+.$$

775 **Reproducibility.** The source code to reproduce the results from Section 2 is
 776 available at <https://gitlab.onelab.info/gmsh/fem>, in the folder
 777 `examples/helmholtzFlow/freefield`. The results from Section 3 are available at
 778 <https://gitlab.onelab.info/gmsh/ddm>, in the folders
 779 `examples/helmholtzflow/waveguide`, `examples/helmholtz/waveguide` and
 780 `examples/helmholtzflow/freefield`. The intake problem from Section 4 is avail-
 781 able in `examples/helmholtzflow/nacelle3D`. Instructions are provided in the cor-
 782 responding README.md files.

783 **Acknowledgments.** Computational resources have been provided by the Con-
 784 sortium des Équipements de Calcul Intensif (CÉCI), funded by the Fonds de la
 785 Recherche Scientifique de Belgique (F.R.S.-FNRS) under Grant No. 2.5020.11 and
 786 by the Walloon Region. The present research benefited from computational resources
 787 made available on Lucia, the Tier-1 supercomputer of the Walloon Region, infras-
 788 tructure funded by the Walloon Region under the grant agreement n°1910247. We
 789 acknowledge LUMI-BE for awarding this project access to the LUMI supercomputer,
 790 owned by the EuroHPC Joint Undertaking, hosted by CSC (Finland) and the LUMI
 791 consortium through a LUMI-BE Regular Access call. LUMI-BE is a joint effort from
 792 BELSPO (federal), SPW Économie Emploi Recherche (Wallonia), Department of
 793 Economy, Science & Innovation (Flanders) and Innoviris (Brussels). This project was
 794 provided with computer and storage resources by GENCI at IDRIS thanks to the
 795 grant 2022-AD010613476 on the supercomputer Jean Zay on the CSL partition. The
 796 authors would like to thank Dr. Jérémie Gaidamour for his useful guidance and help
 797 on the supercomputer Jean Zay.

798 REFERENCES

799 [1] P. AMESTOY, O. BOITEAU, A. BUTTARI, M. GEREST, F. JÉZÉQUEL, J.-Y. L'EXCELLENT, AND
 800 T. MARY, *Mixed precision low-rank approximations and their application to block low-*
 801 *rank LU factorization*, IMA Journal of Numerical Analysis, 43 (2022), pp. 2198–2227,
 802 <https://doi.org/10.1093/imanum/drac037>.

- 803 [2] P. AMESTOY, I. S. DUFF, J. KOSTER, AND J.-Y. L'EXCELLENT, *A fully asynchronous multi-*
804 *frontal solver using distributed dynamic scheduling*, SIAM Journal on Matrix Analysis and
805 Applications, 23 (2001), pp. 15–41, <https://doi.org/10.1137/S0895479899358194>.
- 806 [3] P. R. AMESTOY, A. BUTTARI, J.-Y. L'EXCELLENT, AND T. MARY, *Performance and scalability*
807 *of the block low-rank multifrontal factorization on multicore architectures*, ACM Trans.
808 Math. Softw., 45 (2019), pp. 1–26, <https://doi.org/10.1145/3242094>.
- 809 [4] P. R. AMESTOY, I. S. DUFF, AND J.-Y. L'EXCELLENT, *Multifrontal parallel distributed symmetric*
810 *and unsymmetric solvers*, Computer Methods in Applied Mechanics and Engineering,
811 184 (2000), pp. 501–520, [https://doi.org/10.1016/S0045-7825\(99\)00242-X](https://doi.org/10.1016/S0045-7825(99)00242-X).
- 812 [5] X. ANTOINE, H. BARUCQ, AND A. BENDALI, *Bayliss-Turkel-like radiation conditions on surfaces*
813 *of arbitrary shape*, Journal of Mathematical Analysis and Applications, 229 (1999), pp. 184–
814 211, <https://doi.org/10.1006/jmaa.1998.6153>.
- 815 [6] X. ANTOINE AND C. GEUZAIN, *Optimized Schwarz domain decomposition methods for scalar*
816 *and vector Helmholtz equations*, in Modern Solvers for Helmholtz Problems. Geosystems
817 Mathematics., V. K. Lahaye D., Tang J., ed., Birkhäuser, Cham, 2017, pp. 189–213, https://doi.org/10.1007/978-3-319-28832-1_8.
- 818 [7] R. ASTLEY, R. SUGIMOTO, AND P. MUSTAFI, *Computational aero-acoustics for fan duct propa-*
819 *gation and radiation. Current status and application to turbofan liner optimisation*, Jour-
820 nal of Sound and Vibration, 330 (2011), pp. 3832–3845, [https://doi.org/10.1016/j.jsv.2011.](https://doi.org/10.1016/j.jsv.2011.03.022)
821 [03.022](https://doi.org/10.1016/j.jsv.2011.03.022).
- 822 [8] S. BALAY, S. ABHYANKAR, M. ADAMS, J. BROWN, P. BRUNE, K. BUSCHELMAN, L. DALCIN,
823 A. DENER, V. ELJKHOUT, W. GROPP, ET AL., *PETSc/TAO users manual*, 2023, [https://](https://petsc.org/release/manual/)
824 petsc.org/release/manual/ (accessed 2023/08/21). Revision 3.19.
- 825 [9] H. BARUCQ, N. ROUXELIN, AND S. TORDEUX, *Low-order Prandtl-Glauert-Lorentz based ab-*
826 *sorbing boundary conditions for solving the convected Helmholtz equation with discon-*
827 *tinuous Galerkin methods*, Journal of Computational Physics, 468 (2022), p. 111450,
828 <https://doi.org/10.1016/j.jcp.2022.111450>.
- 829 [10] H. BÉRIOT AND G. GABARD, *Anisotropic adaptivity of the p-FEM for time-harmonic acoustic*
830 *wave propagation*, Journal of Computational Physics, 378 (2019), pp. 234–256, [https://](https://doi.org/10.1016/j.jcp.2018.11.013)
831 doi.org/10.1016/j.jcp.2018.11.013.
- 832 [11] H. BÉRIOT, G. GABARD, AND E. PERREY-DEBAIN, *Analysis of high-order finite elements for*
833 *convected wave propagation*, International Journal for Numerical Methods in Engineering,
834 96 (2013), pp. 665–688, <https://doi.org/10.1002/nme.4559>.
- 835 [12] H. BÉRIOT, A. PRINN, AND G. GABARD, *Efficient implementation of high-order finite elements*
836 *for Helmholtz problems*, International Journal for Numerical Methods in Engineering, 106
837 (2016), pp. 213–240, <https://doi.org/10.1002/nme.5172>.
- 838 [13] C. BOGEY AND C. BAILLY, *Three-dimensional non-reflective boundary conditions for acoustic*
839 *simulations: far field formulation and validation test cases*, Acta Acustica united with
840 Acustica, 88 (2002), pp. 463–471.
- 841 [14] N. BOOTLAND, V. DOLEAN, P. JOLIVET, AND P.-H. TOURNIER, *A comparison of coarse spaces*
842 *for Helmholtz problems in the high frequency regime*, Computers & Mathematics with
843 Applications, 98 (2021), pp. 239–253, <https://doi.org/10.1016/j.camwa.2021.07.011>.
- 844 [15] Y. BOUBENDIR, X. ANTOINE, AND C. GEUZAIN, *A quasi-optimal non-overlapping domain*
845 *decomposition algorithm for the Helmholtz equation*, Journal of Computational Physics,
846 231 (2012), pp. 262–280, <https://doi.org/10.1016/j.jcp.2011.08.007>.
- 847 [16] X. CLAEYS AND E. PAROLIN, *Robust treatment of cross-points in optimized Schwarz*
848 *methods*, Numerische Mathematik, 151 (2022), pp. 405–442, [https://doi.org/10.1007/](https://doi.org/10.1007/s00211-022-01288-x)
849 [s00211-022-01288-x](https://doi.org/10.1007/s00211-022-01288-x).
- 850 [17] B. DESPRÉS, *Méthodes de Décomposition de Domaine pour les Problèmes de Propaga-*
851 *tion d'Ondes en Régime Harmonique*, Thèse, Université Paris IX Dauphine, UER
852 Mathématiques de la Décision, (1991), <http://www.theses.fr/1991PA090032/document>.
- 853 [18] B. DESPRÉS, A. NICOLOPOULOS, AND B. THIERRY, *Corners and stable optimized domain decom-*
854 *position methods for the Helmholtz problem*, Numerische Mathematik, 149 (2021), pp. 779–
855 818, <https://doi.org/10.1007/s00211-021-01251-2>.
- 856 [19] M. EL BOUJAJI, B. THIERRY, X. ANTOINE, AND C. GEUZAIN, *A quasi-optimal domain decom-*
857 *position algorithm for the time-harmonic Maxwell's equations*, Journal of Computational
858 Physics, 294 (2015), pp. 38–57, <https://doi.org/10.1016/j.jcp.2015.03.041>.
- 859 [20] B. ENGQUIST AND A. MAJDA, *Absorbing boundary conditions for the numerical simulation*
860 *of waves*, Mathematics of Computation, 31 (1977), pp. 629–651, [https://doi.org/10.2307/](https://doi.org/10.2307/2005997)
861 [2005997](https://doi.org/10.2307/2005997).
- 862 [21] B. ENGQUIST AND L. YING, *Sweeping preconditioner for the Helmholtz equation: moving*
863 *perfectly matched layers*, Multiscale Modeling & Simulation, 9 (2011), pp. 686–710,
864

- 865 <https://doi.org/10.1137/100804644>.
- 866 [22] Y. A. ERLANGGA, *Advances in iterative methods and preconditioners for the Helmholtz equa-*
867 *tion*, Archives of Computational Methods in Engineering, 15 (2008), pp. 37–66, <https://doi.org/10.1007/s11831-007-9013-7>.
- 868 [23] O. G. ERNST AND M. J. GANDER, *Why it is difficult to solve Helmholtz problems with classical*
869 *iterative methods*, Numerical Analysis of Multiscale Problems, (2012), pp. 325–363, https://doi.org/10.1007/978-3-642-22061-6_10.
- 870 [24] W. EVERSMAAN, *The boundary condition at an impedance wall in a non-uniform duct with*
871 *potential mean flow*, Journal of Sound and Vibration, 246 (2001), pp. 63–69, <https://doi.org/10.1006/jsvi.2000.3607>.
- 872 [25] G. GABARD, H. BÉRIOT, A. PRINN, AND K. KUCUKCOSKUN, *Adaptive, high-order finite-element*
873 *method for convected acoustics*, AIAA Journal, 56 (2018), pp. 3179–3191, <https://doi.org/10.2514/1.J057054>.
- 874 [26] M. GANDER, F. MAGOULES, AND F. NATAF, *Optimized Schwarz methods without overlap for*
875 *the Helmholtz equation*, SIAM Journal on Scientific Computing, 24 (2002), pp. 38–60,
876 <https://doi.org/10.1137/S1064827501387012>.
- 877 [27] M. J. GANDER AND H. ZHANG, *A class of iterative solvers for the Helmholtz equation: Factor-*
878 *izations, sweeping preconditioners, source transfer, single layer potentials, polarized traces,*
879 *and optimized Schwarz methods*, SIAM Review, 61 (2019), pp. 3–76, <https://doi.org/https://doi.org/10.1137/16M109781X>.
- 880 [28] D. GELDER, *Solution of the compressible flow equations*, International Journal for Numerical
881 *Methods in Engineering*, 3 (1971), pp. 35–43, <https://doi.org/10.1002/nme.1620030107>.
- 882 [29] C. GEUZAINÉ AND J.-F. REMACLE, *Gmsh: A 3-d finite element mesh generator with built-in pre-*
883 *and post-processing facilities*, International journal for numerical methods in engineering,
884 79 (2009), pp. 1309–1331, <https://doi.org/10.1002/nme.2579>.
- 885 [30] M. E. GOLDSTEIN, *Aeroacoustics*, McGraw-Hill Book Company, Inc. New York, 1976.
- 886 [31] T. HAGSTROM, S. HARIHARAN, AND D. THOMPSON, *High-order radiation boundary conditions*
887 *for the convective wave equation in exterior domains*, SIAM Journal on Scientific Comput-
888 *ing*, 25 (2003), pp. 1088–1101, <https://doi.org/10.1137/S1064827502419695>.
- 889 [32] K. HAMICHE, S. LE BRAS, G. GABARD, AND H. BÉRIOT, *Hybrid numerical model for acoustic*
890 *propagation through sheared flows*, Journal of Sound and Vibration, 463 (2019), p. 114951,
891 <https://doi.org/10.1016/j.jsv.2019.114951>.
- 892 [33] L. HÖRMANDER, *The Analysis of Linear Partial Differential Operators III: Pseudo-Differential*
893 *Operators*, Springer, 2007, <https://doi.org/10.1007/978-3-540-49938-1>.
- 894 [34] F. Q. HU, M. E. PIZZO, AND D. M. NARK, *On the use of a Prandtl-Glauert-Lorentz transfor-*
895 *mation for acoustic scattering by rigid bodies with a uniform flow*, Journal of Sound and
896 *Vibration*, 443 (2019), pp. 198–211, <https://doi.org/10.1016/j.jsv.2018.11.043>.
- 897 [35] A. IOB, R. ARINA, AND C. SCHIPANI, *Frequency-domain linearized euler model for turboma-*
898 *chinery noise radiation through engine exhaust*, AIAA journal, 48 (2010), pp. 848–858,
899 <https://doi.org/10.2514/1.J050084>.
- 900 [36] G. KARYPIS AND V. KUMAR, *A fast and highly quality multilevel scheme for partition-*
901 *ing irregular graphs*, SIAM Journal on Scientific Computing, 20 (1999), pp. 359–392,
902 <https://doi.org/10.1137/S1064827595287997>.
- 903 [37] S. LE BRAS, G. GABARD, AND H. BÉRIOT, *Direct and adjoint problems for sound propagation*
904 *in non-uniform flows with lined and vibrating surfaces*, Journal of Fluid Mechanics, 953
905 (2022), p. A16, <https://doi.org/10.1017/jfm.2022.949>.
- 906 [38] Y. LI, R. BROSSIER, AND L. MÉTIVIER, *3D frequency-domain elastic wave modeling with the*
907 *spectral element method using a massively parallel direct solver*, Geophysics, 85 (2020),
908 pp. T71–T88, <https://doi.org/10.1190/geo2019-0172.1>.
- 909 [39] A. LIEU, P. MARCHNER, G. GABARD, H. BÉRIOT, X. ANTOINE, AND C. GEUZAINÉ, *A non-*
910 *overlapping Schwarz domain decomposition method with high-order finite elements for*
911 *flow acoustics*, Computer Methods in Applied Mechanics and Engineering, 369 (2020),
912 p. 113223, <https://doi.org/10.1016/j.cma.2020.113223>.
- 913 [40] M. J. LIDTHILL, *On sound generated aerodynamically I. General theory*, Proceedings of
914 *the Royal Society of London. Series A. Mathematical and Physical Sciences*, 211 (1952),
915 pp. 564–587, <https://doi.org/10.1098/rspa.1952.0060>.
- 916 [41] P.-L. LIONS, *On the Schwarz alternating method. III: a variant for nonoverlapping subdo-*
917 *main*, in Third International Symposium on Domain Decomposition Methods for Partial
918 *Differential Equations*, vol. 6, SIAM Philadelphia, PA, 1990, pp. 202–223.
- 919 [42] Y. Y. LU, *Some techniques for computing wave propagation in optical waveguides*, Communi-
920 *cations in Computational Physics*, 1 (2006), pp. 1056–1075.
- 921 [43] A. MAJDA AND S. OSHER, *Reflection of singularities at the boundary*, Communications on

- 927 Pure and Applied Mathematics, 28 (1975), pp. 479–499, <https://doi.org/10.1002/cpa.3160280404>.
- 928
- 929 [44] P. MARCHNER, *Non-reflecting boundary conditions and domain decomposition methods for*
- 930 *industrial flow acoustics*, PhD thesis, Universités de Lorraine et Liège, 2022, <https://www.theses.fr/2022LORR0094> (accessed 2023/08/21).
- 931
- 932 [45] P. MARCHNER, X. ANTOINE, C. GEUZAINÉ, AND H. BÉRIOT, *Construction and numerical as-*
- 933 *essment of local absorbing boundary conditions for heterogeneous time-harmonic acous-*
- 934 *tic problems*, SIAM Journal on Applied Mathematics, 82 (2022), pp. 476–501, <https://doi.org/10.1137/21M1414929>.
- 935
- 936 [46] P. MARCHNER, H. BÉRIOT, X. ANTOINE, AND C. GEUZAINÉ, *Stable perfectly matched layers with*
- 937 *Lorentz transformation for the convected Helmholtz equation*, Journal of Computational
- 938 Physics, 433 (2021), p. 110180, <https://doi.org/10.1016/j.jcp.2021.110180>.
- 939 [47] V. MATTESI, M. DARBAS, AND C. GEUZAINÉ, *A quasi-optimal non-overlapping domain de-*
- 940 *composition method for two-dimensional time-harmonic elastic wave problems*, Journal of
- 941 Computational Physics, 401 (2020), p. 109050, <https://doi.org/10.1016/j.jcp.2019.109050>.
- 942 [48] F. A. MILINAZZO, C. A. ZALA, AND G. H. BROOKE, *Rational square-root approximations*
- 943 *for parabolic equation algorithms*, The Journal of the Acoustical Society of America, 101
- 944 (1997), pp. 760–766, <https://doi.org/10.1121/1.418038>.
- 945 [49] A. MODAVE, C. GEUZAINÉ, AND X. ANTOINE, *Corner treatments for high-order local absor-*
- 946 *bing boundary conditions in high-frequency acoustic scattering*, Journal of Computational
- 947 Physics, 401 (2020), p. 109029, <https://doi.org/10.1016/j.jcp.2019.109029>.
- 948 [50] A. MODAVE, A. ROYER, X. ANTOINE, AND C. GEUZAINÉ, *A non-overlapping domain de-*
- 949 *composition method with high-order transmission conditions and cross-point treatment*
- 950 *for Helmholtz problems*, Computer Methods in Applied Mechanics and Engineering, 368
- 951 (2020), p. 113162, <https://doi.org/10.1016/j.cma.2020.113162>.
- 952 [51] W. MOHRING, *A well posed acoustic analogy based on a moving acoustic medium*, sep 2010,
- 953 <https://arxiv.org/abs/1009.3766>.
- 954 [52] M. MYERS, *On the acoustic boundary condition in the presence of flow*, Journal of Sound and
- 955 Vibration, 71 (1980), pp. 429–434, [https://doi.org/10.1016/0022-460X\(80\)90424-1](https://doi.org/10.1016/0022-460X(80)90424-1).
- 956 [53] L. NIRENBERG, *Pseudodifferential Operators and Some Applications*, in CBMS Regional Con-
- 957 *ference Series in Mathematics*, vol. 17, AMS, 1973, pp. 19–58.
- 958 [54] É. PAROLIN, *Non-overlapping domain decomposition methods with non-local transmission op-*
- 959 *erators for harmonic wave propagation problems*, PhD thesis, Institut Polytechnique de
- 960 Paris, 2020, <https://www.theses.fr/2020IPPAE011> (accessed 2023/08/21).
- 961 [55] C. PECHSTEIN, *A unified theory of non-overlapping Robin–Schwarz methods: Continuous and*
- 962 *discrete, including cross points*, Journal of Scientific Computing, 96 (2023), p. 60, <https://doi.org/10.1007/s10915-023-02248-9>.
- 963
- 964 [56] Z. PENG AND J.-F. LEE, *A scalable nonoverlapping and nonconformal domain decomposition*
- 965 *method for solving time-harmonic Maxwell equations in r^3* , SIAM Journal on Scientific
- 966 Computing, 34 (2012), pp. A1266–A1295, <https://doi.org/10.1137/100817978>.
- 967 [57] A. D. PIERCE, *Wave equation for sound in fluids with unsteady inhomogeneous flow*, The
- 968 Journal of the Acoustical Society of America, 87 (1990), pp. 2292–2299, <https://doi.org/10.1121/1.399073>.
- 969
- 970 [58] S. W. RIENSTRA AND A. HIRSCHBERG, *An Introduction to Acoustics*, 2004, <https://www.win.tue.nl/~sjoerdr/papers/boek.pdf> (accessed 2023/08/21).
- 971
- 972 [59] A. ROYER, E. BÉCHET, AND C. GEUZAINÉ, *Gmsh-Fem: An Efficient Finite Element Library*
- 973 *Based On Gmsh*, in 14th World Congress on Computational Mechanics (WCCM) & EC-
- 974 COMAS Congress, 2021, <https://doi.org/10.23967/wccm-eccomas.2020.161>.
- 975 [60] A. ROYER, C. GEUZAINÉ, E. BÉCHET, AND A. MODAVE, *A non-overlapping domain decompo-*
- 976 *sition method with perfectly matched layer transmission conditions for the Helmholtz equa-*
- 977 *tion*, Computer Methods in Applied Mechanics and Engineering, 395 (2022), p. 115006,
- 978 <https://doi.org/10.1016/j.cma.2022.115006>.
- 979 [61] P. SOLIN, K. SEGETH, AND I. DOLEZEL, *Higher-Order Finite Element Methods*, Chapman and
- 980 Hall/CRC, 2003, <https://doi.org/10.1201/9780203488041>.
- 981 [62] E. SPIESER, *Adjoint-based jet noise propagation model for the acoustic potential*, PhD thesis,
- 982 Université de Lyon, 2020, <https://www.theses.fr/2020LYSEC043> (accessed 2023/08/21).
- 983 [63] É. SPIESER AND C. BAILLY, *Sound propagation using an adjoint-based method*, Journal of Fluid
- 984 Mechanics, 900 (2020), p. A5, <https://doi.org/10.1017/jfm.2020.469>.
- 985 [64] C. C. STOLK, *A rapidly converging domain decomposition method for the Helmholtz equation*,
- 986 Journal of Computational Physics, 241 (2013), pp. 240–252, <https://doi.org/10.1016/j.jcp.2013.01.039>.
- 987
- 988 [65] M. E. TAYLOR, *Pseudodifferential Operators*, Princeton University Press, 1981.

- 989 [66] B. TESTER, F. ARNOLD, S. CARO, AND S. LIDOINE, *TURNEX: turbomachinery noise radiation*
990 *through the engine exhaust. Publishable Final Activity Report*, EU Project no, 516079
991 (2008).
- 992 [67] B. THIERRY, A. VION, S. TOURNIER, M. EL BOUAJAJI, D. COLIGNON, N. MARSIC, X. ANTOINE,
993 AND C. GEUZAINÉ, *GetDDM: An open framework for testing optimized Schwarz meth-*
994 *ods for time-harmonic wave problems*, *Computer Physics Communications*, 203 (2016),
995 pp. 309–330.
- 996 [68] A. TONNOIR AND M. J. GANDER, *Analysis of Schwarz methods for convected Helmholtz like*
997 *equations*, 2023, <https://hal.science/hal-04038452> .
- 998 [69] J. TYLER AND T. SOFRIN, *Axial flow compressor noise studies*, *Society of Automotive Engineers*
999 *Transactions*, 70 (1962), pp. 309–332, <https://doi.org/10.4271/620532>.
- 1000 [70] A. VION AND C. GEUZAINÉ, *Double sweep preconditioner for optimized Schwarz methods applied*
1001 *to the Helmholtz problem*, *Journal of Computational Physics*, 266 (2014), pp. 171–190,
1002 <https://doi.org/10.1016/j.jcp.2014.02.015>.
- 1003 [71] M. WILLIAMSCHEN, G. GABARD, AND H. BÉRIOT, *Impact of the mean flow representation on*
1004 *DGM simulations of flow acoustics*, in 22nd AIAA/CEAS Aeroacoustics Conference, 2016,
1005 p. 2974, <https://doi.org/10.2514/6.2016-2974>.